Master Thesis

Time-Variability of the Galactic Positron Annihilation Signal

Rudi Reinhardt

Würzburg, October 2025

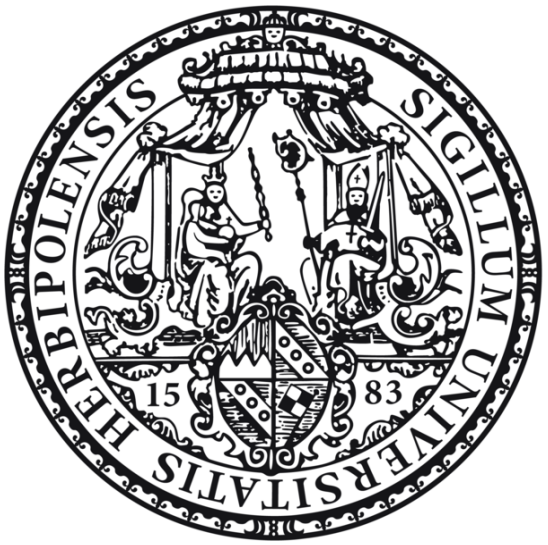

Julius-Maximilians-Universität Würzburg
Faculty of Physics and Astronomy

Supervisors: Dr. Thomas Siegert, Prof. Dr. Matthias Kadler

Abstract

The interactions of low-energy cosmic-rays with asteroids might lead to a measurable variable γ-ray foreground emission within our Solar System. Siegert [2024] modeled the spatial distribution of all relevant asteroid populations, including the Main Belt Asteroids, Jovian and Neptunian Trojans, as well as the Kuiper Belt to determine their density profiles and calculate their appearances by line-of-sight integrations. The signal is expected to vary in time due to the relative motion of Earth and the asteroids. In addition, the Solar cycle will enhance and suppress the signal on an 11 yr timescale. In this work we are using INTEGRAL/SPI data to search for this time-variable foreground albedo in both, the 511 keV line and the ortho-Positronium continuum. We are using 20 yr of data, including high-latitude observations, and covering almost two orbits of Jupiter and its trojans around the Sun, giving us the best opportunity to search for such a signal. Because the signals are expected to vary in time, a standard analysis is not possible for which reason, we split the dataset into monthly parts to calculate the expected responses and recombine them for a global fit. Since the Galaxy is bright in the bulge at 511 keV, we can determine its variability on a two year timescale, which allows us to constrain the possible contributions from all asteroid families and constrain the low-energy cosmic-ray population in the Solar System. We find no significant emission signal for all considered populations. There is indication of time variability in the positron annihilation signal from the center of the Milky Way. However, in contrast to previous observations we find a significant 511 keV line flux of $\mathrm{F}_{511\,\mathrm{keV}} = (8.7 \pm 1.3)\,10^{-5}\,\mathrm{ph\,cm^{-2}\,s^{-1}}$ in the vicinity of the Galactic center, which may mimic variable diffuse emission unless its time variability is taken into account. We also performed simulations with `GEANT4` of electromagnetic and hadronic interactions of cosmic-rays with with asteroids modeled as different sized iron spheres to provide new estimates on albedo fluxes at the Earth. On this way, we are also introducing a new scaling method with a focus on the asteroids rim, where the most interactions take place. Our results coincide with previous calculations of De Gaetano et al. [2023], with fluxes being several orders of magnitude smaller than previously estimated.

Zusammenfassung

Die Wechselwirkungen niederenergetischer kosmischer Strahlen mit Asteroiden könnten zu einer messbaren, variablen Vordergrundemission im γ-Bereich innerhalb unseres Sonnensystems führen. Siegert [2024] modellierte die räumliche Verteilung aller relevanten Asteroidenpopulationen, einschließlich des Hauptgürtels, der Trojaner von Jupiter und Neptun sowie des Kuipergürtels, um deren Dichteprofile zu bestimmen und ihre Erscheinungen am Himmel durch Sichtlinienintegration zu berechnen. Es wird erwartet, dass das Signal aufgrund der relativen Bewegung von Erde und Asteroiden zeitlich variiert. Zusätzlich wird das Signal auf der elfjährigen Zeitskala des Sonnenzyklus verstärkt bzw. abgeschwächt. In dieser Arbeit verwenden wir INTEGRAL/SPI-Daten, um nach dieser zeitlich variablen Vordergrund-Albedo sowohl in der 511-keV-Linie als auch im Ortho-Positronium-Kontinuum zu suchen. Wir nutzen 20 Jahre an Daten, darunter Beobachtungen hoher galaktischer Breiten, die fast zwei Orbits des Jupiters und seiner Trojaner um die Sonne abdecken. Da erwartet wird, dass die Signale zeitlich variieren, ist eine Standardanalyse nicht möglich. Deshalb haben wir den Datensatz in monatliche Abschnitte aufgeteilt und nach Berechnung der erwarteten Detektorantworten diese für einen globalen Fit wieder kombiniert. Da die Galaxie im Bulge hell bei 511 keV ist, können wir ihre Variabilität auf einer zweijährigen Zeitskala bestimmen, was uns erlaubt, die möglichen Beiträge aller Asteroidenfamilien abzuschätzen und die Population niederenergetischer kosmischer Strahlen im Sonnensystem einzuschränken. Wir finden kein signifikantes Emissionssignal für alle betrachteten Populationen. Es gibt jedoch Hinweise auf zeitliche Variabilität im Positronen-Annihilationssignal aus dem Zentrum der Milchstraße. Im Gegensatz zu früheren Beobachtungen finden wir einen signifikanten 511-keV-Linienfluss von $\mathrm{F}_{511\,\mathrm{keV}} = (8.7 \pm 1.3)\,10^{-5}\,\mathrm{ph\,cm^{-2}\,s^{-1}}$ in der Nähe des galaktischen Zentrums. Ohne Berücksichtigung seiner Zeitvariabilität könnte dieses Signal eine variable diffuse Emission vortäuschen. Wir haben Ausßerdem Simulationen (mit `GEANT4`) elektromagnetischer und hadronischer Wechselwirkungen von kosmischen Strahlen mit Asteroiden durchgeführt, die als unterschiedlich große Eisenkugeln modelliert wurden, um neue Abschätzungen des Albedo-Flusses auf der Erde zu berechnen. Auf diesem Wege stellen wir auch eine neue Skalierungsmethode mit Fokus auf den Asteroidenrand vor, wo die meisten Wechselwirkungen stattfinden. Unsere Ergebnisse stimmen mit vorherigen Berechnungen von De Gaetano et al. [2023] überein, wobei die Flüsse um mehrere Größenordnungen kleiner sind als zuvor angenommen.

Contents

1 Introduction

Even after 50 years of observation, the 511 keV signal from the center of the Milky Way is not fully understood yet. It originates from positron-electron annihilation, but we cannot explain the large amount of positrons seen today [Siegert, 2023]. A possible contribution might be the interactions of low-energy cosmic-rays (CRs) with bodies of different sizes within our Solar System producing γ-rays. This also includes the creation of positrons and the associated annihilation line at 511 keV. Previous analyses of the Galactic positron annihilation signal did not include the possible contribution of different asteroid populations in the Solar System in their models. The difficulty here lies in the fact that the γ-ray albedo of asteroids varies over time due to their motion along the ecliptic. In addition, there is further variability on the 11-year timescale due to the Solar cycle. The modulation of the heliosphere protects the inner Solar System from Galactic CRs and thus suppresses positron production. The time variability on different time scales and the weakness of the signal make the development of a model very challenging. Siegert [2024] determined the spatial distribution of all relevant asteroid populations, including the Main Belt Asteroids, the Jovian and Neptunian trojans, as well as the Kuiper Belt Objects and calculated their appearances by line-of-sight integrations. Based on this work, we use his templates to search for the asteroids' γ-ray signal. For this purpose, we use a 20 yr dataset from INTEGRAL/SPI (Vedrenne et al. [2003] and Winkler et al. [2003]), which was taken between 2003 and 2023. We focus on the energy of positron annihilation between 400 and 520 keV.

Several publications have now been released that provide estimates and predictions for the strength of Solar System γ-ray foreground. Moskalenko and Porter [2008] calculated the γ-ray albedo of the Moon before using the emission template in a subsequent paper to also calculate flux expectations for various asteroid populations [Moskalenko et al., 2008], by scaling it to smaller sizes and larger distances. For all the relevant asteroid populations within the Solar System cumulated, they calculated a total 511 keV line flux along the ecliptic of $\sim 5 \cdot 10^{-4}\,\mathrm{ph\,cm^{-2}\,s^{-1}}$. Depending on energy, Solar activity and time (because of the relative motion of the asteroids to the Earth), we expect the Galactic positron annihilation signal to be weaker by 0.1–20 % due to the ecliptic overlap of several asteroid populations with the Galactic plane and bulge [Siegert, 2024]. Such a flux, however, would still be within reach for INTEGRAL/SPI.

This thesis is structured as follows: in Chp. 2, we describe the origin of the Galactic

511 keV line by looking at the life cycle of positrons. Chp. 3 focuses on the Solar System γ-ray foreground with focus on the interactions between CRs and asteroids. Chp. 4 shows how INTEGRAL/SPI data are generally processed and analyzed. We look at the underlying model behind the fit and will adjust the background for our dataset. In Chp. 5, we search for a point source near the Galactic center and examine its time-variability. Chp. 6 is devoted to the analysis of the extended sources. We analyze lightcurves of the Galactic components as well as for the different asteroid populations. In Chp. 7, we present our own simulations of CR interactions. Finally, we discuss our findings (Chp. 8) and conclude in Chp. 9.

2 Galactic 511 keV emission in Astronomy

This first chapter deals with the 511 keV electron-positron annihilation signal in general. To start with, we first take a look at previous observations, starting with the Oriented Scintillation Spectrometer Experiment (OSSE) [Purcell et al., 1997]. These observations show an enhancement of emission at positive latitudes above the Galactic center. This structure, often referred to as the 'OSSE fountain', is still an unexplained mystery, as its origin is still unknown. We also take a look at the work of Siegert et al. [2016]. They used a dataset of over ten years of observations with INTEGRAL/SPI to constrain characteristic spectral shapes for different spatial components in the Galactic disk and bulge. Their models are also used in this master thesis. The observations are followed by a theoretical overview of the 511 keV γ-ray line. We will look at the various processes that are responsible for the formation of positrons. After cooling down to the eV scale, the positrons annihilate in various processes, usually under formation of the intermediate state of positronium. We will also look at this phenomenon, as it has important effects on the observed 511 keV line.

2.1 Previous Observations

2.1.1 OSSE

Over the last 50 years the Galactic 511 keV signal has been measured with multiple instruments. After the pioneering balloon experiments of the 1960s and 1970s [Haymes et al., 1969], the first satellite experiments such as OSSE revealed the morphology of the emission signal, showing its 'diffuse' character.
Purcell et al. [1997] combined observations of the Galactic plane and Galactic center region of the OSSE instrument onboard the Compton Gamma-Ray Observatory (CGRO) spacecraft(1991-1997) with scanning observations by the Transient Gamma-Ray Spectrometer (TGRS) and Solar Maximum Mission (SMM) instruments to produce maps of the Galactic narrow 511 keV positron annihilation line radiation. The OSSE image showed a positive latitude enhancement with a γ-ray line flux of $(5.4 \pm 1.5) \cdot 10^{-4}\,\mathrm{ph\,cm^{-2}\,s^{-1}}$ in a region roughly defined by a 2D Gaussian centered at $\ell = (-1.1 \pm 2.0)^\circ$, b $= (9.0 \pm 1.3)^\circ$

(Fig. 1). The image was reconstructed by using Singular Value Decomposition (SVD). They also used the Maximum Entropy Method [Narayan and Nityananda, 1986] resulting in a similar feature.

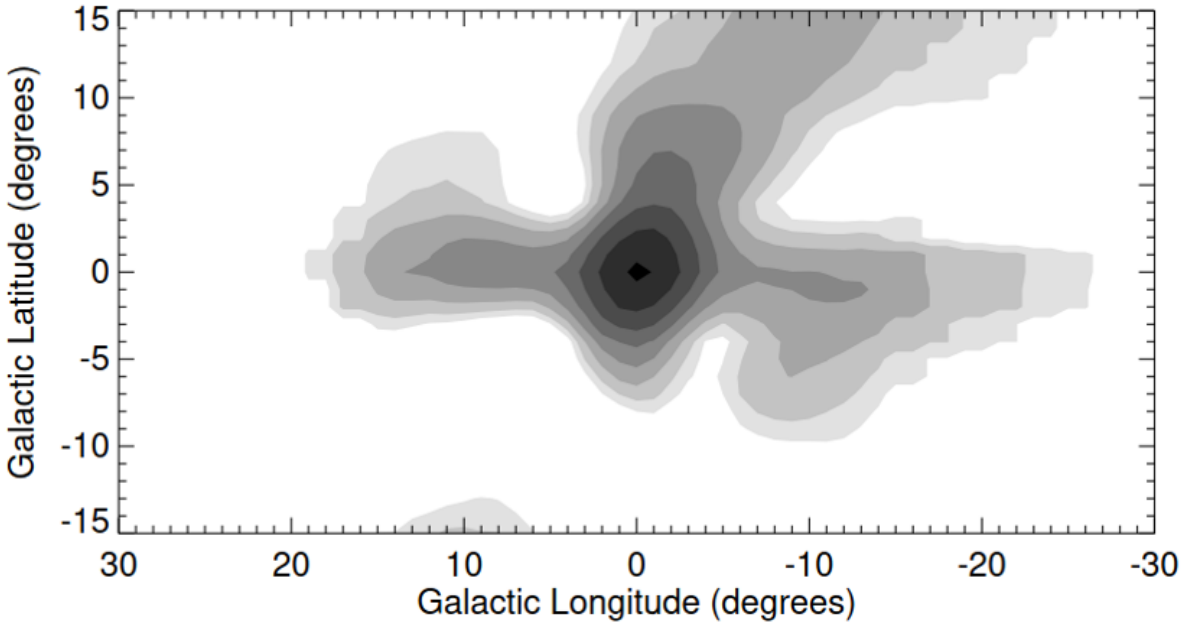

Fig. 1: Map of the Galactic 511 keV signal reconstructed with the SVD method [Purcell et al., 1997].

This 'OSSE-fountain' was discussed in the context of positron production by supernovae and the jet activity of Sgr A*, but was later refuted as an image artifact, in particular because the follow-up mission INTEGRAL was unable to detect either such a feature for positive latitudes or a 511 keV disk in the first years of its observation with short exposure time [Knödlseder et al., 2005]. However, combing 20 years of INTEGRAL/SPI data, and more than 25 years after the first OSSE image, Yoneda et al. [2025] found a similar positive latitude enhancement. The flux they measured is on the order of $\sim 4 \cdot 10^{-5}\,\mathrm{ph\,cm^{-2}\,s^{-1}}$, i.e. a factor of $\sim$ 13 smaller than the OSSE fountain. This may again point out a time variable feature.

2.1.2 INTEGRAL/SPI Observations

Today, the latest information about the Galactic 511 keV emission are gathered from the SPI instrument onboard INTEGRAL (Vedrenne et al. [2003] and Winkler et al. [2003]). The latest measurement of 511 keV fluxes in the Galaxy are from Siegert et al. [2022]. For the Galactic bulge they find a flux of $\mathrm{F_B} = (8.9 - 10.1) \cdot 10^{-4}\,\mathrm{ph\,cm^{-2}\,s^{-1}}$, for the disk $\mathrm{F_D} = (13.1 - 20.1) \cdot 10^{-4}\mathrm{ph\,cm^{-2}\,s^{-1}}$ and for the Galactic center $\mathrm{F_{GCS}} = (0.6 - 1.2) \cdot 10^{-4}$ $\mathrm{ph\,cm^{-2}\,s^{-1}}$[Siegert, 2023]. The template models used for their fit were taken from Skinner et al. [2014] and Siegert et al. [2016], who performed likelihood analyses and discussions of

these models in their works. The image obtained from SPI at 511 keV is unique compared to other wavelengths and emission processes.

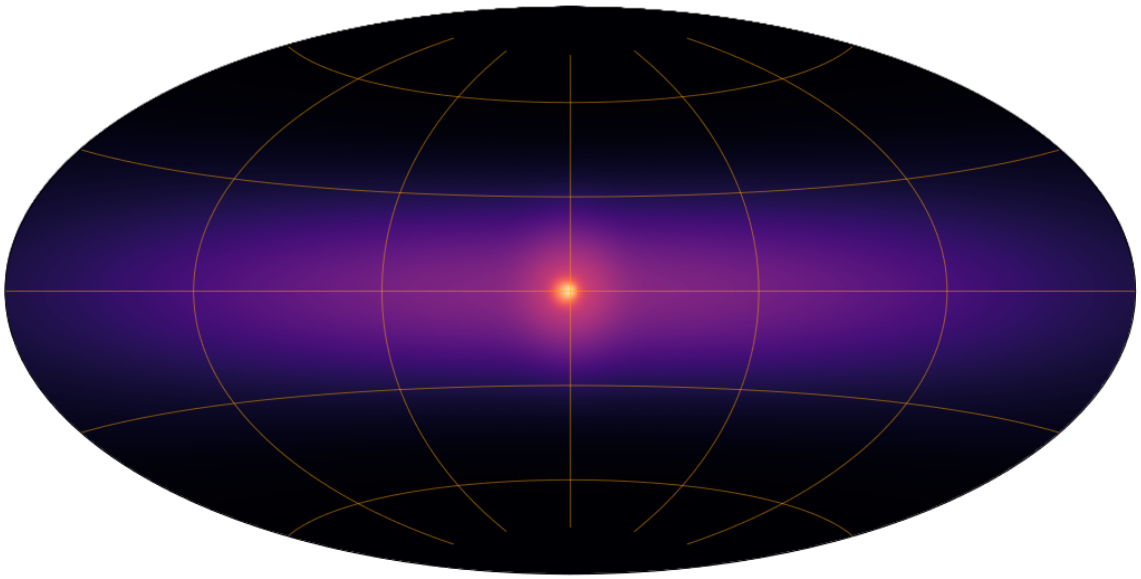

Fig. 2: Resulting image as the Maximum likelihood solution from INTEGRAL/SPI data at 511 keV [Siegert et al., 2016].

Fig. 2 shows a maximum likelihood fit to the raw SPI count data, requiring four components: a disk, and three components to describe the bulge, including a point-like source coincident with the Galactic center. Considering the angular resolution of SPI of 2.7°, this point source covers a diameter of about 400 pc – reminiscent of the entire central molecular zone [Siegert, 2023].
Using this best-fit morphology model, Siegert et al. [2019a] calculated the positron annihilation spectrum of the Galaxy, which can be seen in Fig. 3. In addition to the bright positron annihilation line, there is the ortho-Positronium spectrum below 511 keV. The positronium fraction f_{PS} is measured to be between 0.97 and 1.00. Thus, charge exchange and radiative recombination appear to be the most important annihilation processes, both of which form positronium. We will introduce the different annihilation processes later in Sec. 2.4 and give also further information on the positronium formation and the resulting spectrum in Sec. 2.5.

2.2 Life Cycle of Positrons in our Galaxy

In this section we describe the life cycle of positrons in the Milky Way. Following their production, positrons enter a propagation phase, in which different interactions with matter lead to energy losses. After cooling down to temperatures of their ambient environment, the positrons thermalize with the interstellar medium (ISM), which eventually results in their annihilation with electrons. This happens sometimes directly but mostly (spectral

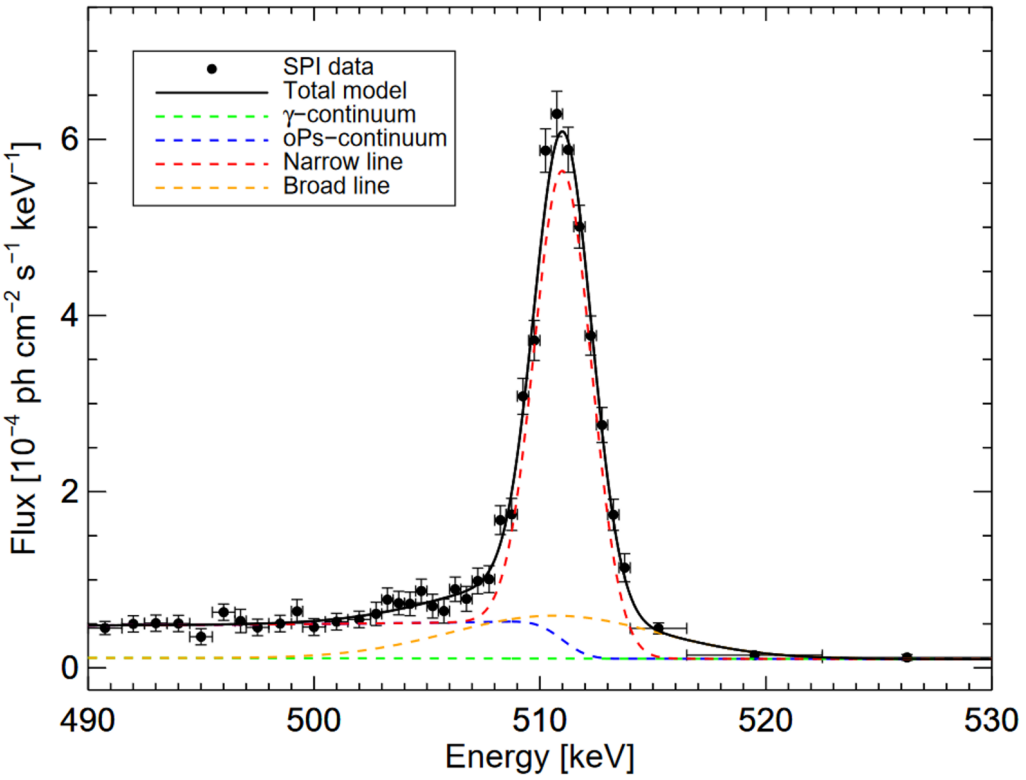

Fig. 3: Positron annihilation spectrum of the Galaxy using the best-fit morphology model of Siegert et al. [2016]. Shown are the SPI data points in black, and four model components: narrow 511 keV line (red), broad 511 keV line (orange), ortho-Positronium continuum (blue), Galactic γ-ray continuum (green). The total model is shown as solid black line [Siegert et al., 2019a].

analyses of the Galactic center reveal a positronium fraction of $f_{PS} = (96.7 \pm 2.2)\%$ [Jean et al., 2005]) via positronium formation. The direct annihilation is also possible in flight. But given the much higher cross section for Positronium formation, this contribution is negligible for this study. The signature of electron-positron annihilation are the 511 keV line and the ortho-Positronium (oPs) spectrum below 511 keV. The line energy and cutoff energy of oPs spectrum corresponds to the rest mass of the particles, conserving energy, mass, momentum, charge and spin.

2.2.1 Formation of Positrons

Positrons in our Galaxy are produced by one of the following processes:

1. The β^+ decay of radioactive nuclei (e.g. ^{26}Al, ^{44}Ti or ^{56}Ni)
2. The decay of π^+ into μ^+, which produces a positron
3. Photon-photon pair production, producing an electron-positron pair
4. Pair production due to a photon interacting with a strong magnetic field

All these processes are found in astrophysical environments: So the first process, the β^+ decay of radioactive nuclei, occurs mainly in novae, supernovae or Wolf-Rayet stars. The decay of π^+ into μ^+ and finally positrons is found in collisions of low-energy CRs with interstellar matter.

The third process (photon-photon interactions) $\gamma + \gamma \rightarrow e^+ + e^-$ requires high-energy photons (threshold energy 1.022 MeV) and thus takes place in the environment of compact objects, such as black holes, micro-quasars or active Galactic nuclei (AGNs). The fourth process requires strong magnetic fields and is found in the vicinity of (highly magnetized) neutron stars. In summary, the main sources of positron formation in our Galaxy are supernovae (SNe), novae, compact objects (neutron stars, black holes, white dwarfs, etc.) and CR Guessoum et al. [2005].

2.3 In-Flight Phase

After their formation, the positrons propagate through the ISM. As charged leptons, they interact via the Coulomb force with other charged particles, namely: electrons, ions, atoms or molecules. Furthermore, they experience the electromagnetic and photon fields of the ISM.

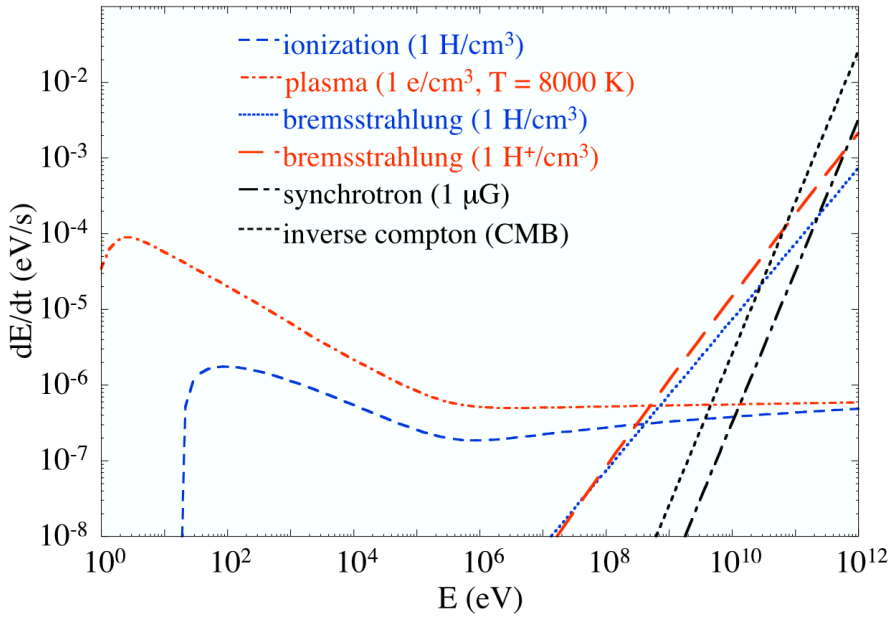

Fig. 4: Positron energy loss rates as a function of positron energy with the conditions of the ISM [Prantzos et al., 2011].

This results in a continuous loss of energy and thus a deceleration of the positrons. The strength of the various interactions depends on the energy of the positrons, the density of the ambient gas and the strength of magnetic fields. Fig. 4 shows the energy loss rates of different processes as a function of positron energy with the conditions of the warm ISM (T=8000 K) [Prantzos et al., 2011]. For positrons of energies $< 500\,\mathrm{MeV}$ only plasma

and ionisation losses are relevant. Plasma losses occur mainly via Coulomb scatterings with free electrons or inelastic interactions with atoms and molecules. These different inelastic reactions produced by positrons and their energy threshold are shown in Table 1. Bremsstrahlung scales with the density of the gas like ionisation and is dominant for positrons with energies of 500 MeV to 10 GeV. Inverse Compton and synchrotron radiation are the dominant energy loss processes for positrons of high energies above ~ 10 GeV.

Process	Threshold (eV)
$e^+ + H \rightarrow Ps + H^+$	6.8
$e^+ + H \rightarrow e^+ + e^- + H^+$	13.6
$e^+ + H \rightarrow e^+ + H^*$	10.2
$e^+ + H \rightarrow e^+ + H^{**}$	12.1
$e^+ + He \rightarrow Ps + He^+$	17.8
$e^+ + He \rightarrow e^+ + e^- + He^+$	24.6
$e^+ + He \rightarrow e^+ + He^*$	21.2
$e^+ + H_2 \rightarrow Ps + H_2^+$	8.6
$e^+ + H_2 \rightarrow e^+ + e^- + H_2^+$	15.4
$e^+ + H_2 \rightarrow e^+ + H_2^*$	12.0

Tab. 1: Reactions of positrons with the ISM and their energy thresholds [Guessoum et al., 2005].

2.4 Thermalisation and Annihilation

Once the positrons have reached the energies of the ambient environment, they are 'thermalized' with the gas. This means that their energy distribution relaxes to a Maxwellian distribution with the temperature of the interstellar gas. The positrons undergo a number of different processes that finally lead to their annihilation, either directly or via positronium formation. The positron reaction rates of those processes are shown in Fig. 5.

2.4.1 Charge Exchange

Positrons interact with an electron (either from H, H_2 or He) to form positronium. In Fig. 5, it can be seen that in the range between $\sim (10^4 - 10^6)$ K, the charge exchange shows the largest interaction cross-section and thus provides the highest annihilation rates. At temperatures below the energy threshold of 6.8 eV (Tab. 1) charge exchange is excluded

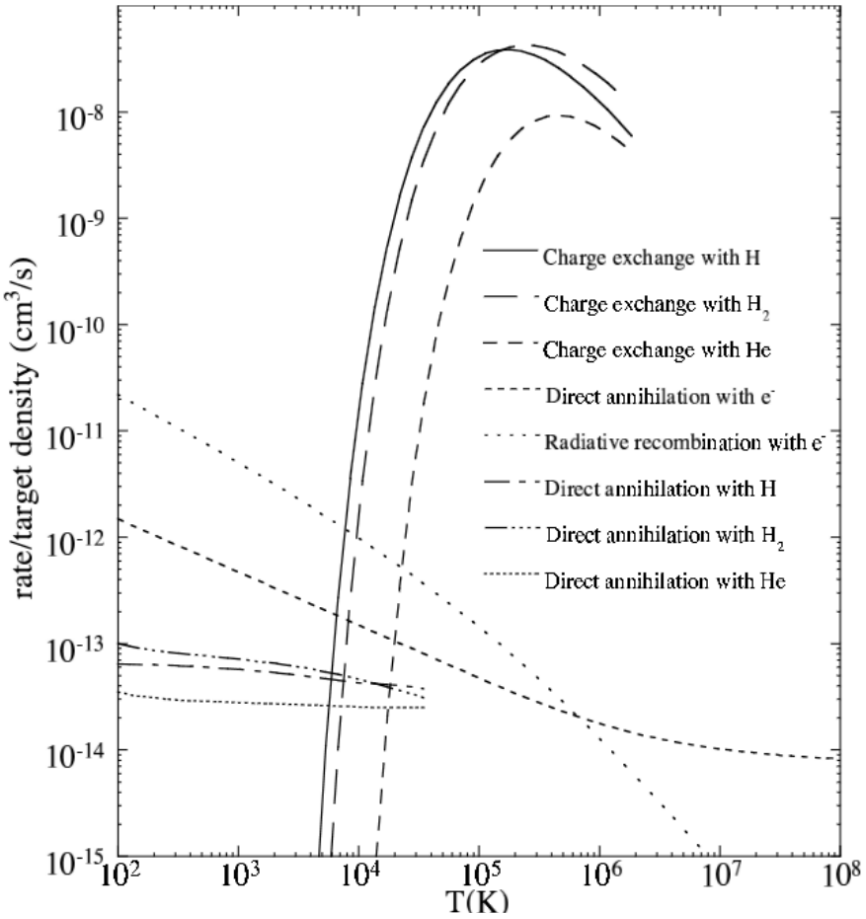

Fig. 5: Positron reaction rates as a function of positron temperature [Guessoum et al., 2005].

and is only possible in the high-energy tail of the Maxwellian distribution. In general, this will be very rare in the cold ISM ($T_{dust} \sim 100$K and $T_{gas} \sim 10$K). It can also not happen in the hot phases of the ISM, where the hydrogen is completely ionized, which explains the cut-off of the annihilation rate at about $5 \cdot 10^6$ K.

2.4.2 Radiative Recombination

In this process, a positron interacts with a free electron and also forms positronium. The cross section is larger than that for charge exchange at temperatures below $\sim 10^4$ K. For this reason radiative recombination is relevant for low temperatures if enough free electrons are available. For high energies/temperatures this process is competing with direct annihilation.

2.4.3 Direct Annihilation

Here, positrons annihilate directly with electrons of the ISM, without the formation of positronium. The cross section is only above that of radiative recombination for temperatures higher than $\sim 10^6$ K.

2.5 Positronium Formation

Positronium (Ps) is a bound state of a positron with an electron. As charge exchange and radiative recombination are dominant (Fig. 5), it plays an important role in the annihilation process. The state of Ps can be treated as the one of hydrogen atom. Depending on the relative orientations of the spins of the positron and the electron, the Ps ground state has two possible spin states. There is a singlet state with antiparallel spins (total spin $S_{tot} = 0$) called para-positronium (pPs). The triplet state for which positron and electron have parallel spins ($S_{tot} = 1$) is known as ortho-positronium (oPs). Following from the (2S+1) spin degeneracy, the pPs state will be formed in 1/4 of the time and the oPs state will be formed in 3/4 of the time. The lifetimes of the different states before annihilation (in vacuum) are $1.2 \cdot 10^{-10}$ s for pPs and $1.4 \cdot 10^{-7}$ s for oPs.
The release of annihilation photons is constrained by conservation of momentum and spin. The pPs releases two photons of 511 keV (as in the case of direct annihilation). The oPs, on the other hand, is forced by spin conservation to create an odd number of photons with a total energy of 1022 keV (due to momentum conservation) producing a continuum of energies up to 511 keV [Prantzos et al., 2011]. For the majority of cases, three photons are created. Fig. 6 shows the oPs annihilation spectrum. One can see the peak (which is also the cut-off) at 511 keV. The number of photons created decreases for lower energies. The pPs spectrum on the other hand looks like the spectrum of direct annihilation, due to the creation of two 511 keV photons.

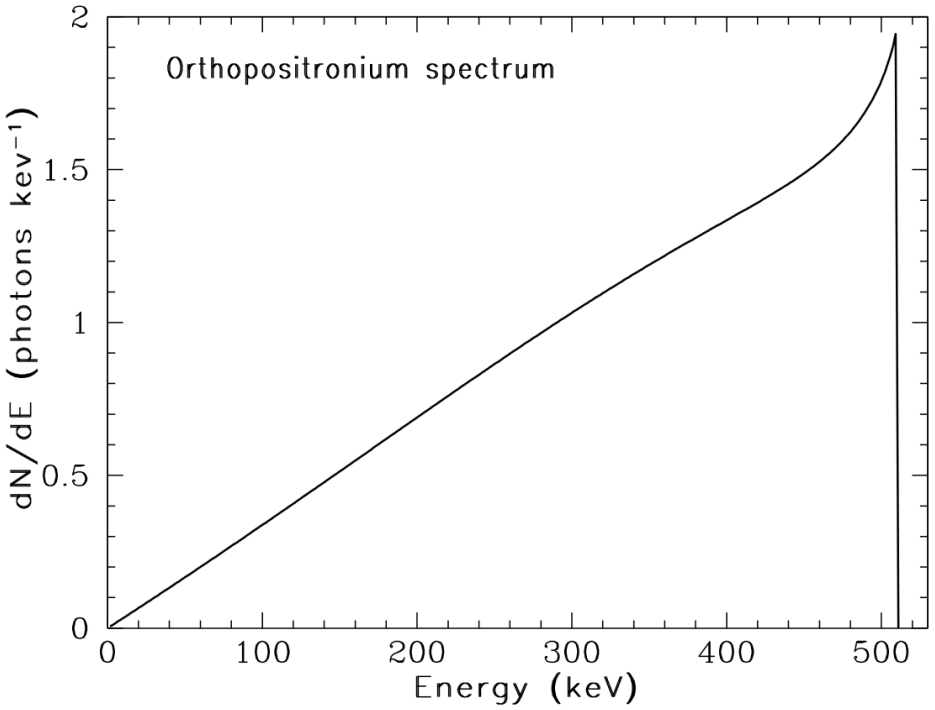

Fig. 6: Three photon spectrum of ortho-Positronium annihilation [Prantzos et al., 2011].

3 Solar System γ-ray Foreground

In addition to the Galactic positron annihilation signal, a foreground component of 511 keV emission also arises within our Solar System. This emission originates from CR interactions with bodies of various sizes distributed throughout the heliosphere. In this chapter, we first review the physical processes underlying this phenomenon, focusing on the origin of the Solar System γ-ray foreground. We then examine the contributions from different asteroid populations, with particular emphasis on the morphology and time variability of their signals. Finally, we discuss the implications of this foreground for the interpretation of measurements of the Galactic positron annihilation signal (see 2.1).

3.1 Interaction of Cosmic Rays with Solar System Bodies

With the launch of sensitive γ-ray instruments, such as Fermi/LAT [Atwood et al., 2009] and INTEGRAL/SPI, several theoretical and simulation-based predictions for the Solar System γ-ray foreground have been published. Moskalenko and Porter [2008], for example, calculated the γ-ray albedo of the Moon using the `GEANT4` Monte Carlo framework to simulate the interactions of CR nuclei with Moon rock. In their later work, the authors used the template of the Moon to also calculate the albedo flux of Small Solar System Bodies (SSSBs) with radii above 100 cm from 0.1 MeV to 10 GeV assuming the flux depends linearly of the radial size r of the bodies [Moskalenko et al., 2008]. This dependency on the asteroids' radii may actually be incorrect, which we will discuss in Chp. 7 of this thesis.

A notable outcome of these simulations was the prediction of secondary positron production through hadronic processes such as:

$$\mathrm{p} + \mathrm{p} \rightarrow \mathrm{p} + \mathrm{p} + \pi^+ + \pi^-$$

$$\pi^+ \rightarrow \mu^+ + \nu_\mu$$

$$\mu^+ \rightarrow \mathrm{e}^+ + \bar{\nu}_\mu + \nu_\mathrm{e}$$

Since the positrons are created inside the dense SSSBs (asteroid densities of $\sim (1 - 4)\,\mathrm{g/cm^3}$ compared to the density of the ISM of $\sim 10^{-24}\,\mathrm{g/cm^3}$), they instantly cool down due to inelastic collisions and by ionizing the material, eventually annihilating at their production

site. This results in γ-rays that could be measured if they escape the SSSBs. Only a rim of a few centimeters of an object may then actually contribute to the γ-ray albedo. The appearance of the observed signal depends on multiple factors, including the morphology (e.g., asteroid belts vs. Trojan clouds), the size and number of contributing objects, and the relative motion of the population with respect to Earth [Siegert, 2023].

3.1.1 Orbital Periods of Selected Solar System Objects

The motion of an object in the sky can also be observed in its γ-ray albedo. The orbital period of the object and thus its distance from the Sun are relevant factors. Tab. 2 shows the orbital periods and distances from the Sun of selected Solar System objects. In addition to the eight planets, a few bodies from the Main Belt, as well as the Kuiper Belt are also shown.

Object	Siderial Period (Orbit) [yr]	Distance from the Sun [AU]	Classification
Mercury	0.24	0.39	Planet
Venus	0.62	0.72	Planet
Earth	1.00	1.00	Planet
Mars	1.88	1.52	Planet
Vesta	3.63	2.36	Asteroid (Main Belt)
Ceres	4.60	2.77	Dwarf planet (Main Belt)
Jupiter	11.86	5.20	Planet
Saturn	29.46	9.58	Planet
Uranus	84.01	19.20	Planet
Neptune	164.79	30.05	Planet
Pluto	247.94	39.48	Dwarf planet (Kuiper Belt)

Tab. 2: Sidereal periods and distances from the Sun of selected Solar System objects.

The orbital periods of Jupiter and Neptune are particularly significant in this context, as each of them hosts an asteroid population. The differences in their orbital velocities (orbit of 11.86 yr for Jupiter compared to 164.79 yr for Neptune) are also reflected in the appearance of their respective asteroid populations.

3.1.2 Modulation by the 11-Year Solar Cycle

Additional to the variation based on the properties of each asteroid population, the intensity of the γ-ray albedo also varies with the 11-year timescale of the Solar cycle. The heliospheric magnetic field, carried outward by charged particles (mostly protons) of the Solar wind, modulates the flux of Galactic CRs entering the Solar System. This modulation is quantified by the Solar modulation potential ϕ, expressed in MV, which characterizes the energy-dependent attenuation of the CR spectrum. During a Solar maximum, ϕ typically exceeds 1000 MV, while values below 500 MV are common during a Solar minimum. Since the inner Solar System is more effectively shielded by the heliosphere, the local flux of Galactic CR - and therefore the positron production rate in asteroid populations - is significantly reduced. In contrast, Trans-Neptunian objects are subject to a much weaker modulation effect and are thus expected to exhibit higher 511 keV γ-ray fluxes. However, some degree of variability in the signal is still expected even at large heliocentric distances [Siegert, 2024]. The effects of this heliocentric modulation on the expected γ-ray flux of different asteroid populations can be seen in Fig. 11.

3.2 Overview of Relevant Asteroid Populations

Siegert [2024] performed 3D-fits to determine the density profiles of different Solar System asteroid populations including the Main-Belt Asteroids (MBA), the Trojans of Jupiter and Neptune (JT and NT), as well as the Kuiper Belt Objects (KBO). This includes also the calculation of the asteroids appearances in γ-rays by line-of-sight integrations. The asteroids distribution within our Solar System is shown in Fig. 7. In the following, we will give a brief overview over the relevant populations, we are focusing on in this work.

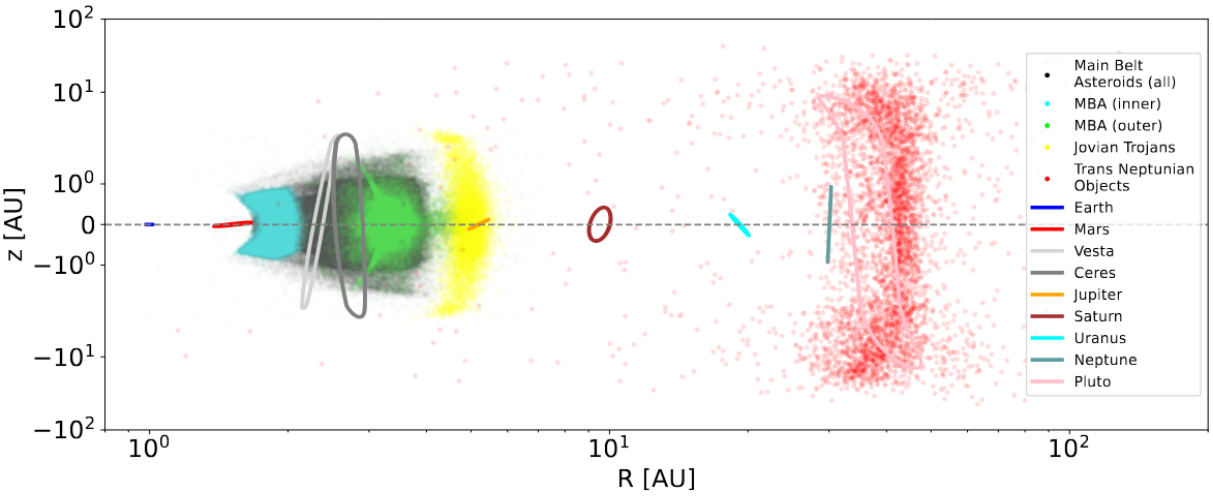

Fig. 7: Distribution of asteroid populations within our Solar System [Siegert, 2024].

3.2.1 Kuiper Belt Objects

The SSSBs between the orbit of Neptune and the presumed inner boundary of the Oort Cloud [Emel'Yanenko et al., 2007] at the edge of our Solar System are commonly grouped under the term Trans-Neptunian Objects (TNOs). Most of these objects are also classified as part of the Kuiper Belt. They are found between 30 and 50 AU with the most objects being around 40 AU. The appearance of the Kuiper Belt is similar to that of the Main Belt between Mars and Jupiter (Fig. 7). While the MBAs exhibit apparent variations in vertical thickness on a 1-year timescale due to Earth's orbital motion, such effects are negligible for the more distant KBOs. Due to the larger number of KBOs and the reduced impact of Solar modulation at these distances (see Sec. 3.1.2: Modulation by the 11-Year Solar Cycle), the γ-ray signal from KBOs is expected to be dominant. Therefore, we adopt the KBO model as a template to represent both the Main Belt and Kuiper Belt signals simultaneously. Fig. 8 shows the KBOs as an example on 01/01/2005 using the template of Siegert [2024].

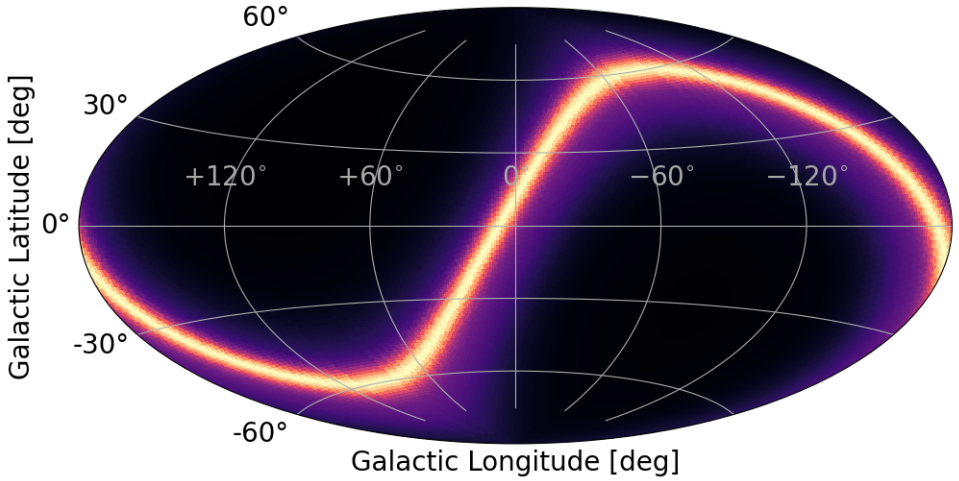

Fig. 8: Appearances of Kuiper Belt Objects shown as an example on 01/01/2005 [Siegert, 2024].

3.2.2 Trojan Objects

We also model the γ-ray albedo from both the JT and NT. The objects in these populations are found in the Lagrange points L4 and L5 of their respective planets. The radial distribution of the JT peak at the orbital distance of Jupiter around 5 AU. Their inclinations range up to 40° with the peak at 12°. Due to the limited number of known NT objects (about 30–40 objects), we adopt the spatial model of the JT and scale it to Neptune's orbit at $\sim$30 AU. Fig. 9 shows the spatial distribution of both trojan populations on 01/01/2005. In contrast to the KBOs (Fig. 8), the JT and NT populations exhibit two distinct concentrations at L4 and L5, which give rise to characteristic features in the expected

γ-ray signal. Because the Earth and the trojan populations move relative to each other, the observed signal is time-dependent. Animations illustrating this effect are provided by Siegert [2024] and can be found at: `https://www.physik.uni-wuerzburg.de/astro/mitarbeiter/ag-siegert/solar-system-gamma-ray-albedo/`. Due to Jupiter's shorter orbital period of 11.86 yr compared to Neptune's 164.79 yr, the apparent motion of the JT-induced signal varies on shorter timescales than that of the NT (Tab. 2).

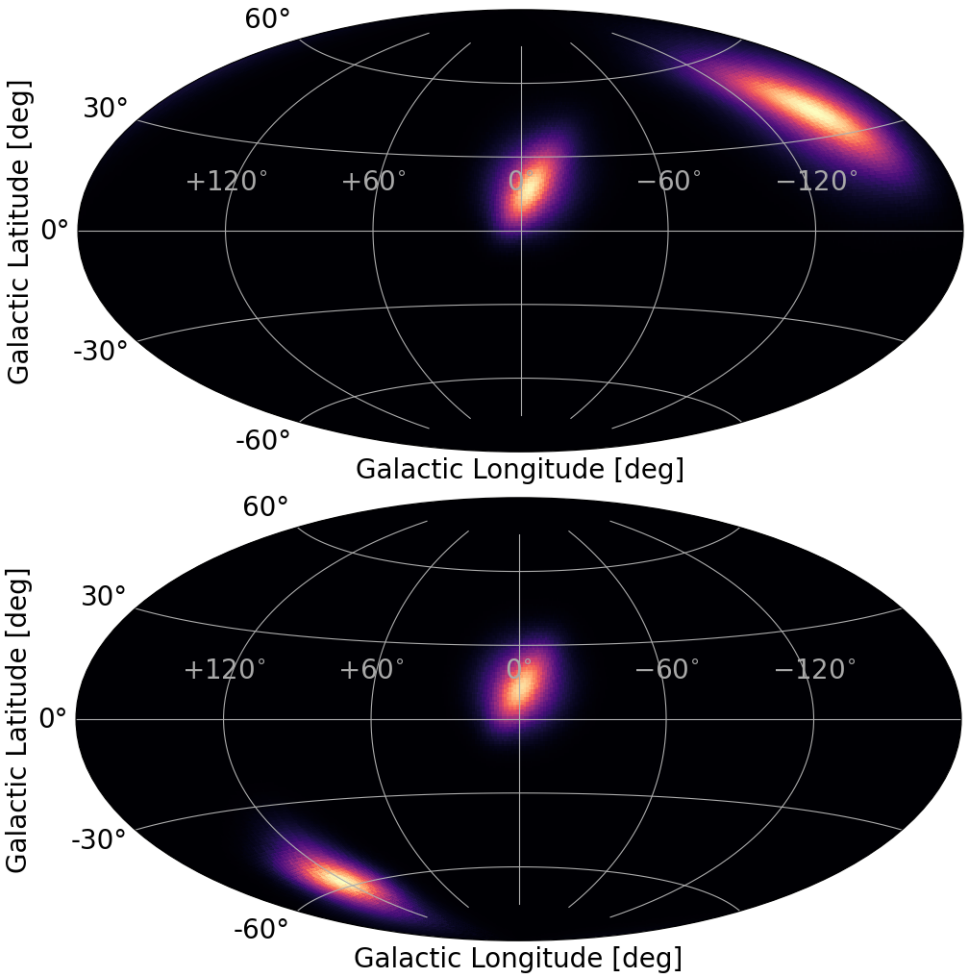

Fig. 9: Appearances of the Jovian Trojans (Top) and Neptunian Trojans (bottom) all shown as an example on 01/01/2005 [Siegert, 2024].

3.3 Flux Expectations and Interpretation of the Signal

According to estimates by Moskalenko et al. [2008], the total 511 keV flux along the ecliptic (KBO+MBA+JT+NT) could be in the order of $\sim 5 \cdot 10^{-4}\,\mathrm{ph\,cm^{-2}\,s^{-1}}$. This is shown in Fig. 10, where their calculated γ-ray albedo spectra for CR nuclei interactions in the Moon rock for selected modulation potentials are visualized. In addition to various nuclear lines, the 511 keV line is also clearly visible.

The effect of heliospheric modulation on positron production and thus directly on the

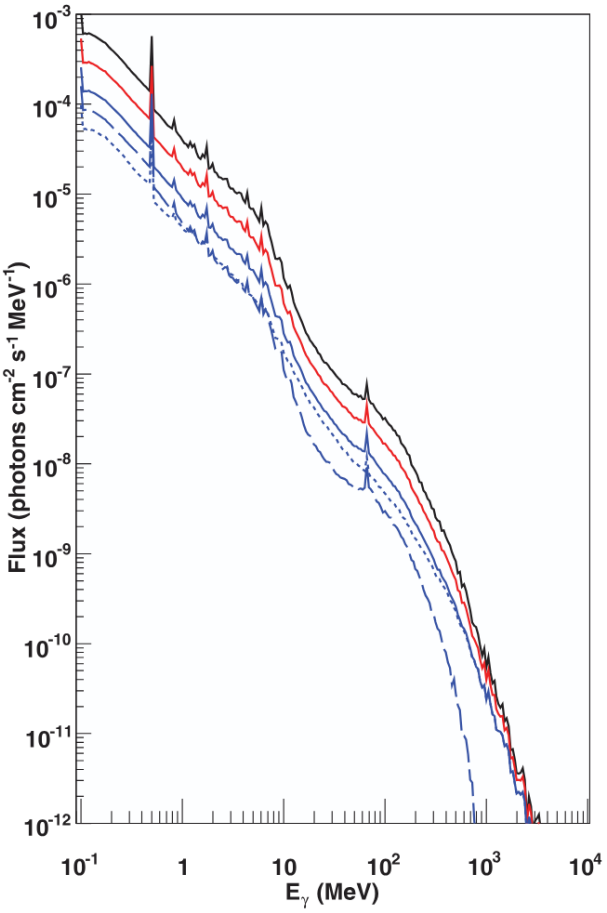

Fig. 10: Calculated γ-ray albedo spectrum for CR nuclei interactions in the Moon rock for selected modulation potentials. Black line: no modulation; red line: $\phi = 500$ MV; blue line: $\phi = 1500$ MV. Dashed and dotted blue lines show the albedo of the disk and the rim, respectively, for the case of $\phi = 1500$ MV [Moskalenko et al., 2008].

γ-ray flux can also be estimated. The flux of Galactic CRs on Earth is steadily measured via a global network of ground-based neutron monitors. From this data, Väisänen et al. [2023] calculated the Solar modulation potential ϕ for combined measurements from 1964 to 2022. From this, the relative flux of the γ-ray albedo of the asteroid populations can now be determined. This can be seen in Fig. 11.

The figure shows the Solar modulation potential ϕ and the expected relative flux in the Galactic bulge of various asteroid populations between 2003 and 2023. In particular, the curves of MBA, KBO and the NT show the increased γ-ray fluxes at low Solar activity, as described in Sec. 3.1.2. Because of their similar appearances, the two curves of MBA and KBO show a very similar trend. But, as also described in Sec. 3.2.1, the MBA curve shows higher variability due to the Earth´s orbital motion, which is not the case for the more distant KBOs. Because of their slow orbit, the NTs have an almost constant fraction of objects overlapping with the Galactic bulge over the whole period, compared to the JT. Nevertheless, the two Solar minima (the first between 2007 and 2010, the second between 2018 and 2022) show different expectations in the bulge flux of the NTs. This is because

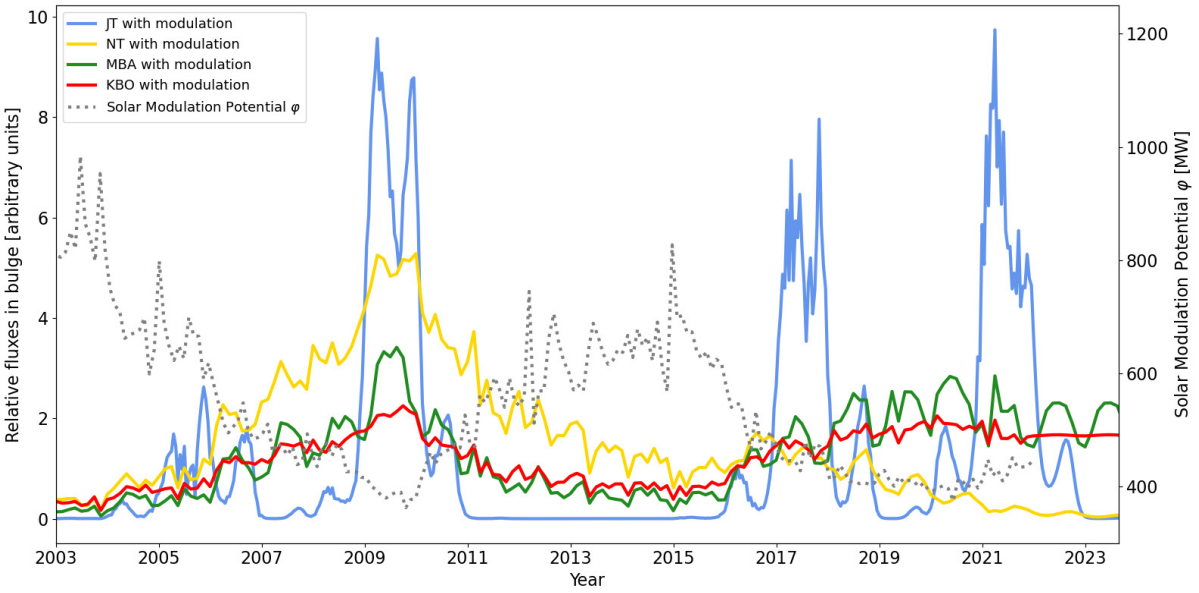

Fig. 11: The Solar modulation potential ϕ (dotted grey line) for from 2003 to 2022 [Väisänen et al., 2023] and the corresponding relative flux in the Galactic bulge (arbitrary units) for different asteroid populations.

between the period of 2010 to 2018 some of its objects moved out of line of sight with the bulge. So, the figure shows also another effect in addition to heliospheric modulation: the fraction of SSSBs overlapping with the Galactic bulge. This is best illustrated by the course of the JT. The two distinct features in L4 and L5 of Jupiter, as well as its orbit of approximately 12 yr, can be seen. So, depending on energy, Solar activity and time (because of the relative motion), the true Galactic emission can be expected to be weaker by 0.1–20 % due to the ecliptic overlap of several asteroid populations with the Galactic plane and bulge [Siegert, 2024]. If these estimates are confirmed by actual observations of the signal, this will have a massive impact on the interpretation of previous measurements of the Galactic 511 keV emission:

According to Siegert [2023], the disk-like feature observed previously (Fig. 2) may not be the Galactic disk, but perhaps halo emission or even foreground. There is also a debate about the rate at which positrons are produced within the Galaxy, how far they propagate, and where they eventually annihilate. Finding answers to these open questions also matters when it comes to assessing various Galactic phenomena: to constrain the production of radioactive isotopes such as ^{26}Al or ^{60}Fe, the number of massive stars and novae, and also dark matter, which is assumed to produce positrons as secondary particles. In addition, the trajectories of the Trojan objects play an important role in interpreting features from previous observations, which were mostly characterized as image artifacts before. One example of this is the above-mentioned OSSE observation with its positive latitude enhancement, the 'OSSE fountain' (Sec. 2.1.1). The OSSE measurements took place between 1991-07-12 and 1997-01-05 [Purcell et al., 1997], a timespan of roughly 2000

days. The Jovian Trojans moved in total 167° across the ecliptic, while the Neptunian Trojans moved by 12°. The apparent epicyclic motion of the Trojans, especially the Jovian Trojans, leads to an uneven distribution of their emissions. As a result, most of the emission during this specific observation period now occurs only at positive latitudes above a certain threshold flux, thus overlapping with the positive latitude enhancement from the OSSE observations. Siegert [2024] used his models for the Jovian and Neptunian Trojans to create single emission templates and also a combined one shown in Fig. 12.

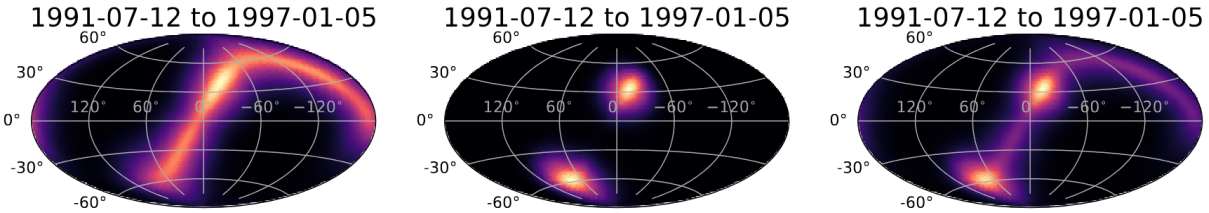

Fig. 12: Cumulative emission of Jovian Trojans (left), Neptunian Trojans (middle), and combined emission (right) from 1991-07-12 to 1997-01-05, i.e. observation times of OSSE according to Purcell et al. [1997]. Especially the Jovian Trojans appear asymmetric along the ecliptic as the observation time is only half the orbital period of Jupiter of 11.86 yr. Furthermore, the apparent epicyclic motion of the trojans creates a positive latitude enhancement [Siegert, 2024].

Due to their shorter orbital period, the Jovian Trojans exhibit an extended emission along the ecliptic compared to the Neptunian Trojans. The epicyclic motion then leads to the formation of brighter features in the emission, one of which can be seen for the Jovian Trojans. In addition, the Neptunian Trojans add emission for latitudes $> 15°$. Together, the combined emission during the OSSE measurements results in a bright spot that could explain the origin of the 'OSSE-fountain'. This would also explain why later follow-up observations with INTEGRAL/SPI were not able to show such a feature [Knödlseder et al., 2005]. By taking all of the above mentioned aspects into account, observing different asteroid populations is of great importance for better understanding the Galactic 511 keV signal.

4 Dataset and Analysis

The following chapter deals with the dataset used in this work and the various analysis tools that are employed. We begin with a brief look at the INTEGRAL mission with the SPI instrument onboard, from which observational data were obtained. We will then provide an overview of the underlying data analysis and also go into more detail about the processing of the instrumental background.

4.1 INTEGRAL/SPI

The International Gamma Ray Laboratory (INTEGRAL, Winkler et al. [2003]) was launched by ESA in October 2002. The scientific mission halted at the end of February 2025, but INTEGRAL will continue to orbit Earth until 2029. During its mission time of two decades, INTEGRAL accumulated an enormous amount of valuable data in hard X-ray and soft γ-rays for the interpretation of high-energy astrophysical phenomena with its four main instruments (Spectrometer on INTEGRAL (SPI), Imager on Board the INTEGRAL Satellite (IBIS), JEM-X Joint European X-ray Monitor (JEM-X), and the Optical Monitoring Camera (OMC)).
The data used in this work is obtained from from SPI, which is a coded mask telescope, described in detail by Vedrenne et al. [2003]. One of the main scientific goals of the mission was the study of cosmic nucleosynthesis using nuclear lines, as well as the observation of the Galactic 511 keV signal, for which its sensitivity in the energy band from 20 to 8000 keV is well suited. As a spectrometer, SPI provides high energy resolution (FWHM at the 511 keV line of (2.16 ± 0.03) keV[Jean et al., 2003]), whereas its imaging is limited compared to other telescopes with an angular resolution of $\sim 2.7°$ and a high background sensitivity. Because of this, INTEGRAL's orbit is highly eccentric (perigee of 9000 km and epogee of 154,600 km) to include long observation times beyond the radiation belts and thus in more-stable background environments [Diehl et al., 2018]. Fig. 13 shows a schematic representation of the SPI instrument design.
The coded mask attached above the 19 Ge detectors can be seen. It restricts the field of view of SPI (from 16° fully coded to 30° partially coded). Each photon source in the sky leaves a unique shadow pattern on the detectors. INTEGRAL/SPI constantly scans the sky in several observation units (pointings). The observation angle changes and the shadow patterns on the detectors adjust accordingly depending on time and/or pointing.

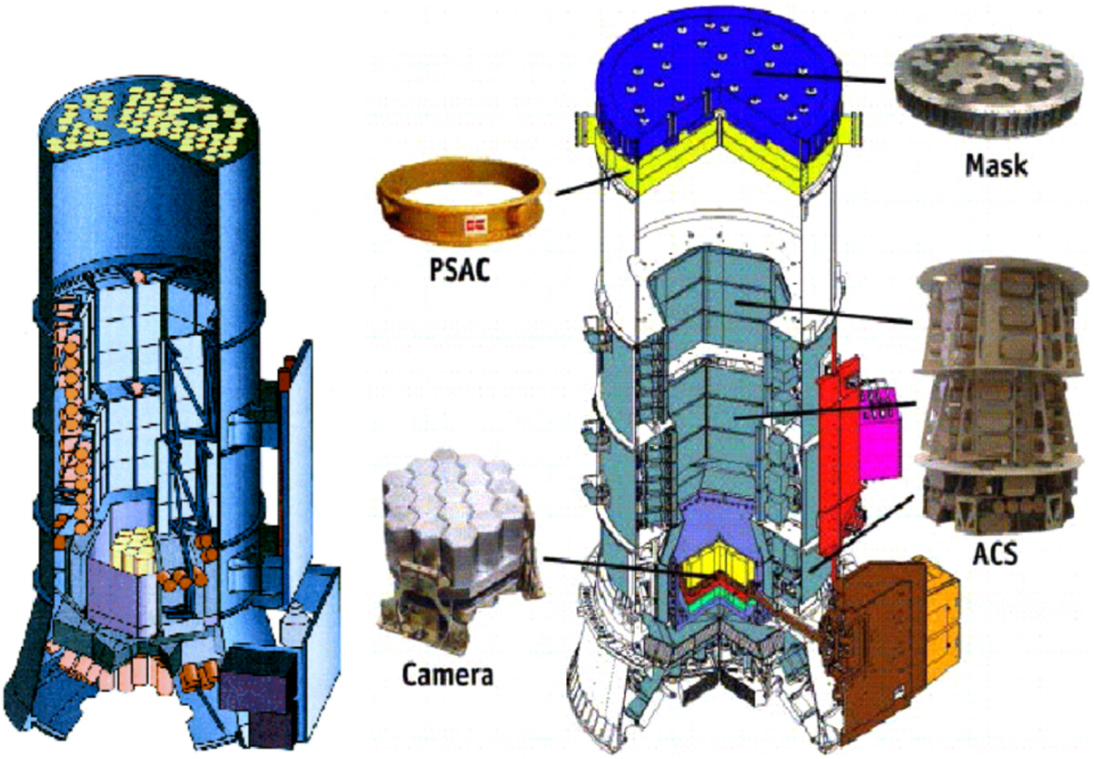

Fig. 13: SPI instrument onboard INTEGRAL, schematic (left) and as a cut-away showing components more clearly (right). Its key elements are the 19 Ge detector camera mounted in a cryostat for operations at ∼80 K, a mask with tungsten elements blocking parts of the field of view for about half of the detectors, and an anti-coincidence detector system (ACS) enclosing the entire instrument and vetoing events from prompt CR interactions, using bismuth germanate (BGO) scintillators and a plastic scintillator plate (PSAC), each with photomultiplier tubes for measuring the scintillation light [Vedrenne et al. [2003] and Diehl et al. [2018]].

This is illustrated in Fig. 14 for the standard INTEGRAL 5 × 5 observation scheme of a point-like source [Siegert et al., 2019b].

The unique shadowgrams are later used to distinguish between background and observed sources in the data. The raw data of the SPI instrument consist of all events that trigger the Ge detectors. In addition to the coded mask, Fig. 13 also shows that the entire instrument is enclosed by an anti-coincidence system (BGO scintillators). Registration of SPI events is vetoed when the anti-coincidence system signals a trigger (window width 725ns), e.g. from a charged particle interaction [Diehl et al., 2018]. This allows the instrument to be shielded from most of the initial background events. With this given geometry, several possible events can now be triggered in one or more of the 19 Ge detectors. Cosmic photons can trigger single events (in one detector) or, through scattering, multiple events (in several detectors). A photon can also be scattered by a detector into the anti-coincidence shield, causing so-called self-vetoed events. Background events can be triggered by CR particles. This happens either promptly through particle interactions with the spacecraft structure or delayed through radioactive de-excitation of previously excited materials in

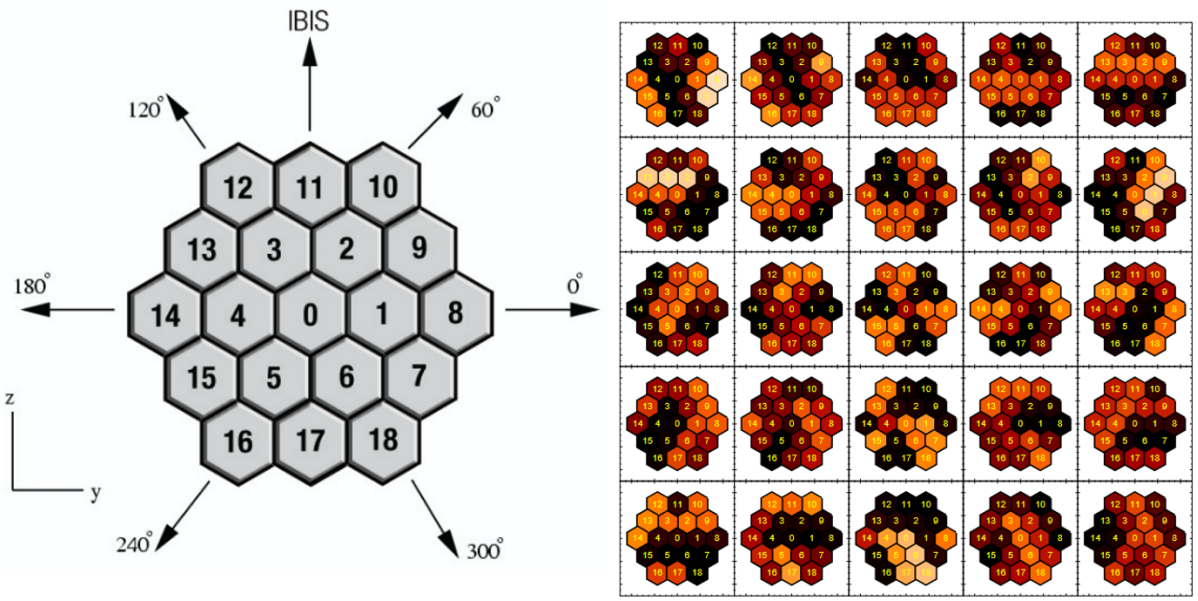

Fig. 14: SPI Ge detector arrangement and shadograms from the mask. The 19 Ge detectors of the SPI camera are arranged in a hexagonal, densely packed, configuration (left). Detectors are numbered inside-out, starting from 0 for the central detector. Shadowgrams are cast by the mask onto the Ge camera. The figure set on the right shows these shadowgrams for a point source on axis, and for the 25 telescope reorientations in steps of 2.1° (pointings) that comprise a standard 5x5 dither pattern. Intensity received by each detector is colour-coded from black (none; shadowed) through red, yellow to white (full exposure) [Diehl et al., 2018].

the spacecraft structure. The parameters measured for each event are: the time of the trigger, the detector identifier and the signal pulse height. For events that triggered more than one of the Ge detectors a corresponding multiple event message includes multiple time tags, detector identifiers and pulse heights [Diehl et al., 2018].
Now that we have provided an overview of the structure of SPI with its geometry and the resulting observation process, we will focus on data analysis in the following section.

4.2 SPI Data Analysis

SPI data analysis typically starts with energy binning. The analysis itself and flux extraction are performed for each, separately treated, energy bin. The smallest possible bin size for SPI data is 0.5 keV. To increase the statistics and to reduce the time for the analysis at the same time, the bin width can be increased. Even if spectral information is lost by doing this, it is convenient out of statistical reasons when analyzing different, especially weak, sources. During a pointing (typically 0.5–1.0 h) and for a specific region in the sky, marked by the Galactic longitude and latitude (ℓ_p/b_p), the satellite is recording data [Siegert et al., 2019b]. Depending on the type of observation (diffuse/pointlike; persistent/transient), N_{Obs} pointings are observed over larger regions in the sky, or only around

the target source. The goal is now to obtain a model of the raw count data per pointing, detector, and energy that combines both the background and the sources of interest in the sky, but also describes them independently of each other. Diehl et al. [2018] and Siegert et al. [2019b] model the data d_p per pointing p for each energy bin individually as

$$m_p = \sum_t \sum_j R_{jp} \sum_{k=1}^{N_S} \theta_{k,t} M_{kj} + \sum_{t'} \sum_{k=N_S+1}^{N_S+N_B} \theta_{k,t'} B_{kp} \quad (1)$$

where M_{kj} is the kth of N_S sky models (celestial emission templates) to which the instrumental response function (IRF, coded mask shadowing) R_{jp} is applied for each pointing p pixelised by j. There are N_B background models B_{kp} which are independent of the IRF in each observation, meaning the background is assumed completely independent from the shadowing of the mask and therefore independent of spacecraft repointing [Siegert et al., 2019b]. The only free parameters are the amplitudes $\theta_{k,t}$ and $\theta_{k,t'}$ of the sky and background models, respectively. All celestial parts and background models depend on different time scales t and t'. While the background timing depends on the instrument materials on various timescales (e.g. as a consequence of Solar activity), the variability of the sky emission is only subject to the physics of the sources themselves. Hereby, the change of $\theta_{k,t'}$ depends on the specific process that resulted in the respective background γ-ray photon. This means changes on short time scales for prompt emission (e.g. after a Solar flare with a high dose of CR particles) or very long scales when the creation of radioactive material happens on shorter timescales than the decay time [Siegert et al., 2019b].

The distribution underlying the dataset D of counting photons into an energy bin is the Poisson statistics. The likelihood $\mathcal{L}(\mathbf{D}/\theta)$ can be determined from this using the model m_p for the data d_p per pointing p.

$$\mathcal{L}(\mathbf{D}/\theta) = \prod_{p=1}^{N_{Obs}} \frac{m_p^{d_p} \exp(-m_p)}{d_p!} \quad (2)$$

The parameters $\theta_{k,t}$ and $\theta_{k,t'}$ are then determined using a maximum likelihood fit. In this work, we used `spimodfit` [Halloin, 2009] to perform these fits.

This approach to data analysis is straight-forward in terms of interpreting fit adequacy with the help of several statistical parameters (likelihood $\mathcal{L}$ or χ^2-values) and thus the physical meaning. Nevertheless, it should be noted that the input of sky models for the various sources in the sky carries a certain bias. There are also image reconstruction algorithms that do not require many assumptions (e.g. Maximum Entropy [Narayan and Nityananda, 1986] or Singular Value Decomposition which were both used by Purcell et al. [1997]). However, these algorithms will always suffer from the small amount of data, which can lead to imaging artifacts or serendipitous detections. Both approaches can lead to

misinterpretations of the data [Siegert, 2024]. Based on the preliminary work of Siegert et al. [2016] and Skinner et al. [2014] (Sec. 2.1.2), as well as the easily interpretable statistical parameters, we will use sky model fitting in this work as well. Eq. 1 shows that the imported images M_{kj} must first be convolved with the response R_{jp} of the telescope before they can be fitted to the raw data.

4.3 Modeling the Background

After discussing the first term of Eq. 1 and explaining the use of the various sky models M_{kj} and their interaction with the instrument (IRF R_{jp}, coded mask shadowing), in this section we turn our attention to the right-hand side of the equation with the modeling of the background B_{kp}. Fig. 15 shows an integrated all-detector spectrum for orbits 43-1730 of INTEGRAL/SPI.

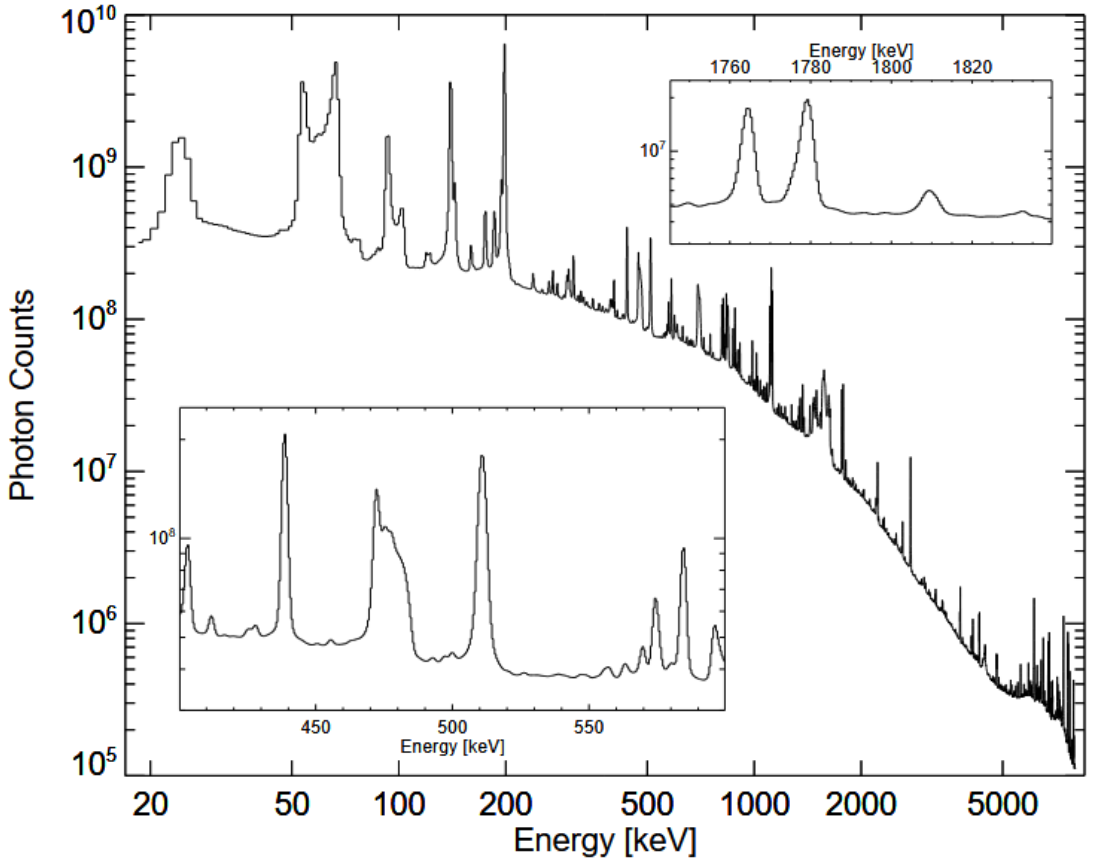

Fig. 15: INTEGRAL/SPI-mission-integrated all-detector spectrum (orbits 43-1730), allowing us to identify even the weakest background features. Inserts show spectral regions near the two brightest celestial lines, the 511 keV line from positron annihilation (lower-left), and the ^{26}Al line at 1809 keV from diffuse nucleosynthesis throughout the Galaxy (upper-right). [Diehl et al., 2018].

A large number of nuclear lines can be seen on top of a broken power law shaped continuum. Most of the background lines are even higher than the brightest celestial lines,

as shown by the two inserts for 511 and 1809 keV. This illustrates how important it is to have a good understanding of the instrumental background and to model it correctly in order to be able to obtain relevant information about the celestial emission from the spectrum.

For this purpose, the SPI spectral BackGround and Response Database (BGRDB) was created and supplied with new data throughout the entire INTEGRAL mission, with consistency checks performed on an ongoing basis. The BGRDB contains fitted spectral parameters per detector/time, both for the continuum and the numerous lines of the instrumental background. The time integration is usually chosen as one INTEGRAL orbit of three days [Siegert et al., 2019b]. Diehl et al. [2018] shows how the decomposition of the spectrum into individual lines works in detail and also illustrates how the BGRDB was maintained during the mission time. They found different families of γ-ray background lines of SPI, characterised by their individual detector patterns: There are the "Ge-like" lines, showing higher count rates for inner detectors (00-06) with respect to the outer ones (07-18). Included are de-excitation lines of nuclei in the SPI camera itself (e.g. Ge and Al), but also produced isotopes (e.g. Ga, Zn and Mg). Other families originate mainly from the material from the spacecraft or the anti-coincidence shield. The "Bi-like" lines show such a pattern with higher count rates for the outer detectors. These include isotopes close to Bi, such as Pb, Ra or Ti.

The most important finding from monitoring the longterm trends in the BGRDB is that the patterns of individual isotopes stay constant on all timescales, also meaning that isotopes that produce different line energies show the same pattern. This confirms the model m_p presented in Eq. 1, in which the response R_{jp} of the instrument has no influence on the background models B_{kp}. In contrast, the product $\sum_j R_{jp} M_{kj}$ changes for each included sky component with each pointing p. The detector patterns of the background B_{kp} depend solely on the underlying physical processes, and thus can be seen as constant $B_{kp} = B_k$. The background model is now divided into continuum B^c and line components B^l, each with the corresponding amplitudes θ^c and θ^l, respectively. These amplitudes do not necessarily contain any information about the underlying physical processes, but may vary over time. Patterns of individual detectors underly also time-variabilities due to changes in their responses, mainly caused by detector degradation and the influence of Solar activity [Siegert et al., 2019b]. The SPI background model including all these considerations for a detector d, energy bin e and a specific pointing p is now written as

$$B_{d,e,p} = \theta^c_{e,p} \times B^c_{d,e,p} + \theta^l_{e,p} \times \sum_{i=i(e)}^{N_{lines}(e)} B^l_{d,e,p} \tag{3}$$

which represents the background $B_{d,e,p}$ as a continuum with $N_{lines}(e)$ individual lines i depending on the respective energy e.

4.4 Dataset and Iterative Background Improvement

Now that we have covered the basics of INTEGRAL/SPI observations and data analysis in the previous sections, with a particular focus on background modeling, we will now focus on the dataset used in this work and attempt to find the best timescale for the re-normalization of the background.

For our analysis we are using a 20 yr dataset from INTEGRAL/SPI, coving the entire sky in the energy range from 400–640 keV in 6 keV bins. The dataset consists of 143,627 pointings with a total exposure time of 369.4 Ms.

The typical integration time for the BGRDB is an INTEGRAL orbit of $\sim 3\,\mathrm{d}$. Therefore, this is also the standard time scale for the re-normalization of the background and thus also for its time variability. However, this does not necessarily have to be optimal. In order to fully model the background, it is necessary not only to formulate a suitable model, but also to find the optimal time variability scale for each energy bin e of a given dataset d. For this reason, we tested different re-normalization times for each energy bin of the above-mentioned dataset. More specifically, in addition to the standard of 3 d, we also tested timescales of 12, 6, 1.5, and 0.75 d. With a smaller timescale for fitting the background, the number of fitted parameters naturally increases significantly. This automatically leads to a reduction in the classical χ^2-values

$$\chi^2 \;=\; \sum_{\mathrm{i}=1}^{\mathrm{N_{Obs}}} \left(\frac{\mathrm{d_i} - \mathrm{m_i}}{\sigma_\mathrm{i}} \right)^2 \tag{4}$$

and thus also leads to better statistics. However, this is based solely on the increase in parameters and does not necessarily mean a better description of the model. Consequently, we need other statistical quantities to compare the different approaches. We use a "modified" χ^2_γ statistics [Mighell, 1999] defined as

$$\chi^2_\gamma \;:=\; \sum_{\mathrm{i}=1}^{\mathrm{N_{Obs}}} \left(\frac{\mathrm{d_i} + \min(\mathrm{d_i}, 1) - \mathrm{m_i}}{\mathrm{d_i} + 1} \right)^2 \tag{5}$$

which replicates the Poisson distribution properties of mean and variance, but avoids the logarithmic and factorial terms for easy computation. As a second and alternative comparison value, we use the Akaike Information Criterion (AIC, Akaike [1974])

$$\mathrm{AIC} \;=\; 2\big(\mathrm{n_{par}} - \ln(\mathcal{L})\big) \tag{6}$$

The AIC penalizes models with a higher number of parameters $\mathrm{n_{par}}$. The χ^2_γ and AIC values are calculated from the best fit value for each energy bin. The χ^2_γ has been specially adapted for Poisson-distributed data. The AIC value of a single model does not provide an absolute statement. However, ΔAIC can be used to compare two or more models,

whereby the minimum and thus the best model is sought [Siegert et al., 2019b]. Fig. 16 shows a comparison of the different background re-normalization timescales for the 511 keV bin (508–514 keV). In addition to the ΔAIC, the red. χ^2 is also plotted

$$\text{red.}\,\chi^2 = \frac{\chi^2_\gamma}{\text{dof}} \tag{7}$$

with dof being the number of degrees of freedom.

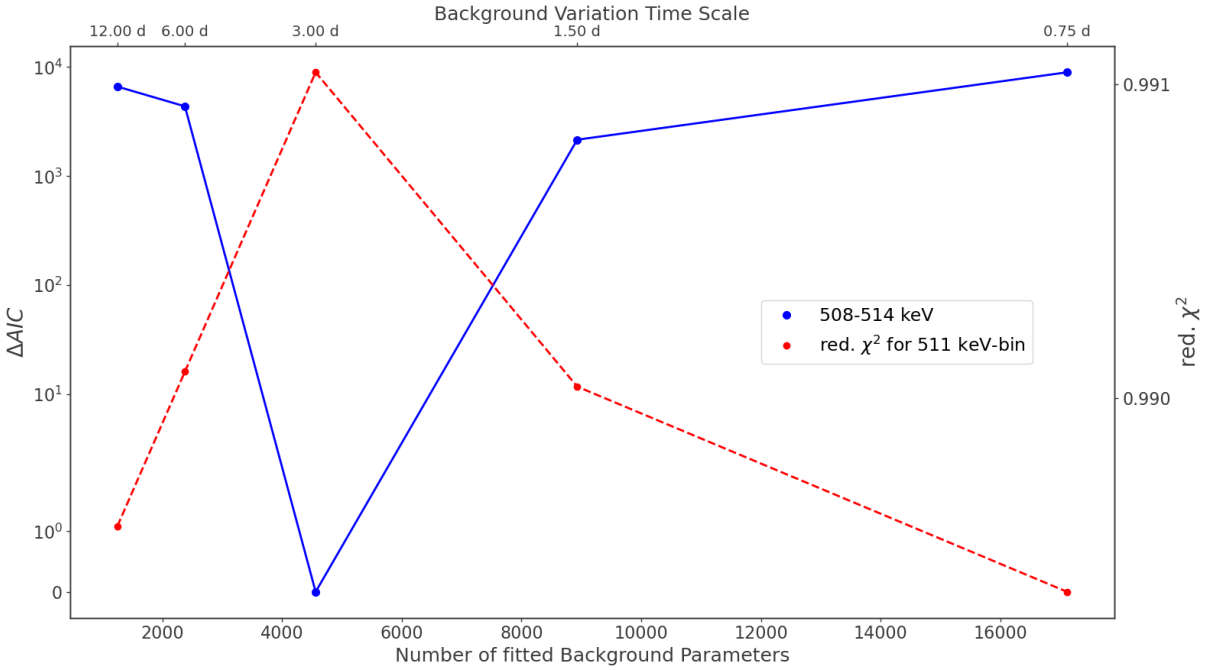

Fig. 16: The red. χ^2 (red) and ΔAIC (blue) values for the tested background variation timescales in the case of the 511 keV energy bin (508-514 keV). Both statistical quantities show the standard model of 3 d re-normalization timescale as the optimal model.

It can be seen that both red. χ^2 and ΔAIC result in the 3 d standard re-scaling period as the optimal fit for the 511 keV bin. We performed this procedure for all energy bins in the range of the dataset from 400–640 keV, leading to the same outcome for all of them, which is reasonable because the total number of photons in each of the 6 keV broad bins is very similar.

Thus, for our dataset, we find that a re-normalization timescale of one INTEGRAL orbit ($\sim$ 3 d) is sufficient for an adequate fit, giving us two fit parameters (continuum + line) for our background model per INTEGRAL orbit. The resulting reduced χ^2 values for all energy bins are typically around 0.990, as shown for the 511 keV bin (Fig. 16). To complete the fit according to the model m_p introduced above (Eq. 1), both the instrumental background and the astrophysical sky components are required. For our 20 yr INTEGRAL/SPI dataset, we have now completed the modeling of the background based on the preliminary works by Diehl et al. [2018] and Siegert et al. [2019b], followed

by the scaling of the background. In the following chapters, we will now deal with celestial emission and the different sky model templates for various astrophysical sources, first for point sources (Chp. 5) and then for extended sources (Chp. 6).

5 Point Source Analysis

To analyze the celestial emission, we now fit various known point sources in the sky. These all contribute to the signal around 511 keV, even if they do not all necessarily show a 511 keV line. In particular, these sources are the Crab, Cyg-X-1, Cen A, SWIFT J1753.5-0127, GRS 1915+105, MR 2251-178, 3C 273 and PSR B1509-58 (Tab. 3).

Point Source	l [°]	b [°]	Classification
Crab	-175.45	-5.79	Pulsar wind nebula / Supernova remnant
Cyg-X-1	71.36	3.06	High-mass X-ray binary
Cen A	-50.49	19.42	Radio galaxy (AGN)
SWIFT J1753.5-0127	24.90	12.18	Low-mass X-ray binary
GRS 1915+105	45.36	-0.22	Microquasar
MR 2251-178	46.17	-61.35	Quasar (AGN, Seyfert 1)
3C 273	-70.00	64.34	Quasar (blazar-like AGN)
PSR B1509-58	-39.69	-1.17	Pulsar wind nebula / Supernova remnant

Tab. 3: Positions (in Galactic coordinates) and classifications of relevant point sources included in our sky model.

5.1 Search for an Additional Point Source

In addition to these eight point sources, previous analyses of the 10 yr INTEGRAL/SPI dataset by Skinner et al. [2014] showed indications of another point source near the Galactic center. They found an offset in the Galactic bulge emission, which was followed by a statistical investigation of the vicinity of the central region. We repeated this process with our 20 yr dataset from INTEGRAL/SPI and searched for statistical evidence of additional point sources near the Galactic center.

We have created test statistics (TS) maps for this purpose. The above-mentioned point sources (Table 3) served as the baseline, as well as the Galactic models of [Siegert et al., 2016] with broad bulge (BB), narrow bulge (NB), and Galactic disk. We will present these models in more detail later (Chp. 6) when we analyze the extended sources. For

$\ell = [\text{-}20°, 20°]$ and $\text{b} = [\text{-}20°, 20°]$, we created such TS maps with a pixelization of 1°. We placed an additional point source at each of these points and calculated the $\Delta\chi^2$ value for each alternative model

$$\Delta\chi^2 \;=\; -2 \cdot \Delta \ln(\mathcal{L}) \;=\; 2\left(\ln \mathcal{L}_2 - \ln \mathcal{L}_1\right) \tag{8}$$

following Wilks' theorem [Wilks, 1938]. We fitted our dataset in three different energy ranges to make assertions about different emission features. We use a broad 511 keV line bin (502–520 keV), an additional energy bin for assessing the oPs emission (400–502 keV) and a bin for the underlying continuum (520–640 keV). Fig 17 shows the TS maps with the $\Delta\chi^2$ values for each energy bin and pixel in a 20×20 grid.

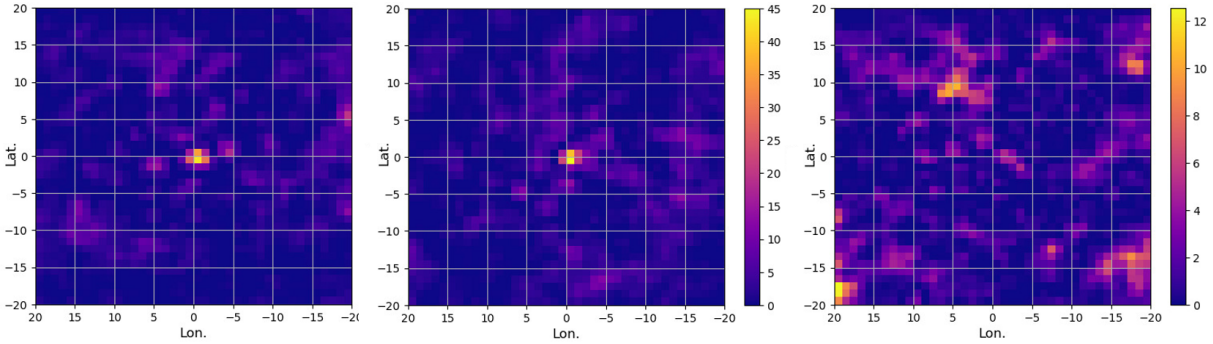

Fig. 17: TS maps for a 20×20 grid showing the $\Delta\chi^2$ values for an additional source at the respective position. The energy range 400–502 keV (left) and 502–520 keV (middle) have the same colorbar and show a very similar pattern with a very bright spot near the Galactic center. The continuum (right), on the other hand, shows a different profile with significantly lower $\Delta\chi^2$ values.

For the energy ranges 400–502 keV and 502-520 keV, similar patterns and their high $\Delta\chi^2$ values around the Galactic center ($\sim$45 for $[\ell, \text{b}] = [\text{-}0.5°, \text{-}0.5°]$) indicate a statistically very significant emission signal in that region. However, this alone is not sufficient to prove the offset [Skinner et al., 2014] of the bulge emission and thus also not to prove the necessity of additional sources at all. If the underlying emission comes directly from the Galactic center without an offset, then an adjustment in the parameters of the Galactic sky model components that are symmetric around the center (e.g. higher amplitude for one of the bulge components) would also be sufficient for a better fit and therefore not require any additional point source. But, the coarse grid with the large field tested in this case shows that other sources further away from the Galactic center cannot be considered as potential point sources in our model. The continuum energy range (520–640 keV) shows a statistically much lower significance than the two bins that are linked to the positron annihilation signal. It can therefore be assumed that the bright points on these two TS maps are indeed positron annihilation features.

Since sources further away from the Galactic center are now excluded, we have significantly reduced the observed area and refined the grid at the same time. So we created TS maps

(same energy ranges) for $\ell = [-2.5°, 2.5°]$ and $b = [-2.5°, 2.5°]$ with pixels of 0.25° each. The results (illustrated in Fig. 18) show a diffuse structure that is consistent with the size of a point source with SPI.

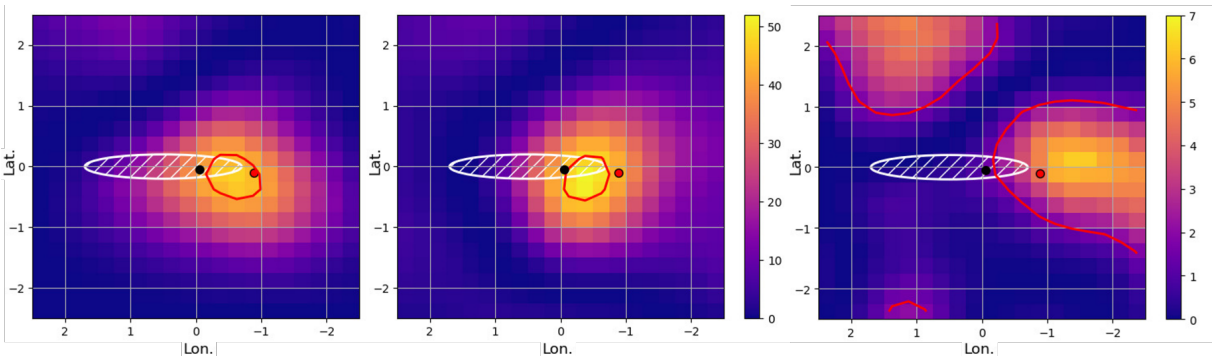

Fig. 18: TS maps for the 2.5×2.5 grid showing again $\Delta\chi^2$ valuesas before in Fig. 17. Again, the energy ranges 400–502 keV (left) and 502–520 keV (middle) have the same colorbar and show very similar results. The Central Molecular Zone (CMZ, white ellipse) as well as two potential sources that are close to the statistical maximum (highest $\Delta\chi^2$ value) are shown. These are Sgr A* (black dot) and 1E1740.7-2942, also known as the Great Annihilator (GA, red dot). The 90% confidence interval ($\Delta\chi^2_{\text{max}} - 4.61$) is also shown in red. The 520–640 keV energy range shows again a different pattern with much smaller $\Delta\chi^2$ values indicating the previous impression that there must be an additional positron annihilation source to be confirmed.

In agreement with the findings of Skinner et al. [2014], the $\Delta\chi^2$ values show an offset from the Galactic center in the bulge emission. The figure also shows the Central Molecular Zone (CMZ), a region in the center of the Milky Way ($\ell = [-0.7°, 1.7°]$, $b = [-0.2°, 0.2°]$), which consists of a complex of giant molecular clouds.
Within the CMZ is also the supermassive black hole located almost exactly in the center of our Galaxy, Sgr A* ($[\ell, b] = [-0.06°, -0.05°]$). The second point source is 1E1740.7-2942 ($[\ell, b] = [-0.884°, -0.106°]$), a microquasar and one of the brightest X-ray emitters near the Galactic center. Both are potential additional point sources for our model. There are both statistical and physical arguments for choosing one of them, which we will weigh up in the next section.

5.2 The Legendary Comeback of the Great Annihilator

In order to compare our results with those of Skinner et al. [2014] as best as possible, we zoom in a little further toward the Galactic center in Fig. 18, specifically to the region $\ell = [-1°, 1°]$, $b = [-1°, 1°]$. Here, we focus only on the TS maps of the energy range of the oPs and the positron annihilation line emission, 400-502 and 502-520 keV respectively, as these provide the highest statistical significance for an additional point source.

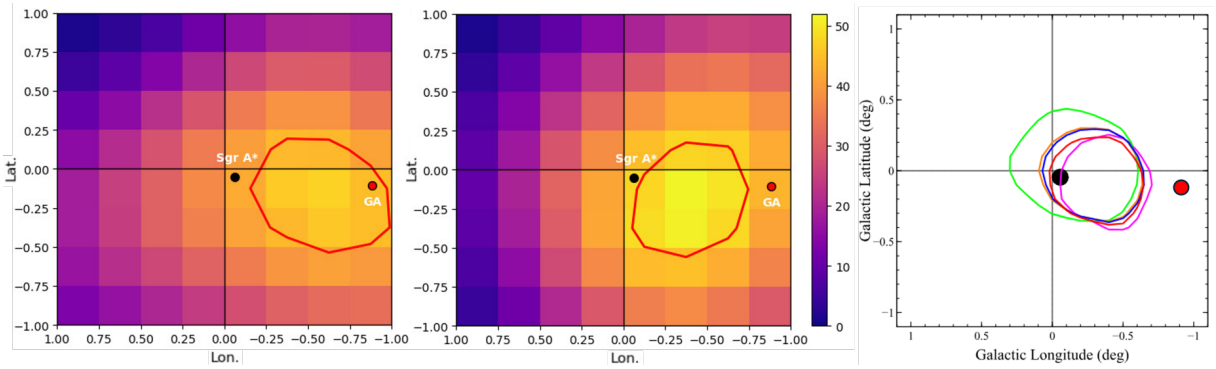

Fig. 19: Central region of the Galaxy from TS maps for oPs (left) and 511 keV line (middle) emission from Fig. 18 in comparison with the previous findings of the 10 yr INTEGRAL/SPI dataset (right, Skinner et al. [2014]). All panels show the position of Sgr A* (black) and 1E1740.7-2942 (red). The 90% confidence interval is marked in any plot with contours at $\Delta\chi^2_{\mathrm{max}} - 4.61$, in the case of Skinner et al. [2014] for different background models. These intervals show consistent results in the statistical analysis of the data for both cases.

Fig. 19 shows strong agreement with previous statistical analyses by Skinner et al. [2014] of the 10 yr INTEGRAL/SPI dataset. For the oPs emission, the statistically most significant location is found at $[\ell, \mathrm{b}]$=[-0.625°, -0.125°] with a $\Delta\chi^2$ of 47.27. The pixel within which Sgr A* is located (angular distance of 0.099°) shows a $\Delta\chi^2$ of 42.16 and thus a difference of 5.11 from the maximum value, being equivalent to 1.79σ. The pixel including 1E1740.7-2942 (angular distance of 0.021°) shows a $\Delta\chi^2$ value of 44.80 and thus a deviation of 2.47, or 1.04σ, from the maximum and is therefore within the 90% confidence interval.
The $\Delta\chi^2$ maximum in the case of the 511 keV bin appears at $[\ell, \mathrm{b}]$=[-0.375°, -0.125°] with a value of 51.23. The Sgr A* pixel lies within the 90% confidence interval with a deviation of 3.48 (1.35σ), while 1E1740.7-2942 has a difference of 7.60, equivalent to 2.3σ.
We further combined our results for the oPs component with those of the 511 keV line emission, yielding a TS map that covers the full positron annihilation energy range of 400–520 keV (see Fig. 20). The resulting 90% confidence region is narrower than in the separate analyses and excludes both Sgr A* and 1E1740.7-2942. The $\Delta\chi^2$ maximum appears at $[\ell, \mathrm{b}]$=[-0.375°, -0.125°] with a value of 97.52. The Sgr A* pixel shows a deviation of 7.60 (2.3σ), while 1E1740.7-2942 has a difference of 9.09, equivalent to 2.6σ.

Statistically, arguments can be found for both sources as potential emitters of a positron annihilation signal, although their close proximity (the angular distance between Sgr A* and 1E1740.7-2942 is 0.83°) and the closely spaced grid should be treated with caution, considering the SPI angular resolution of ∼2.7°. However, it was shown that separating sources within the angular resolution is possible by statistical means (in model space). A final decision cannot be made here for statistical reasons alone. Skinner et al. [2014]

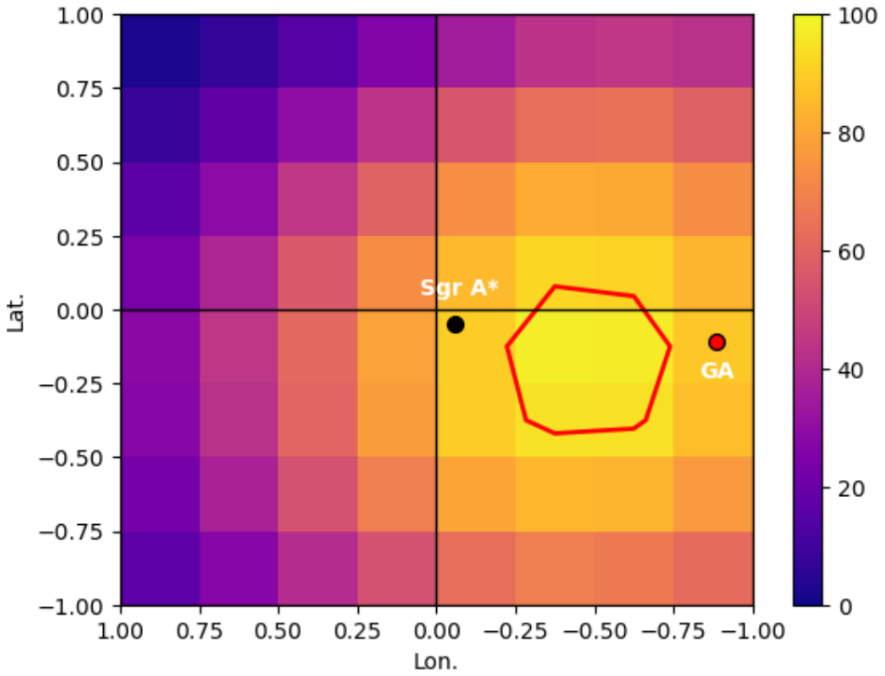

Fig. 20: Combined TS map for the Central region of the Galaxy for the energy range of 400-520 keV. The positions of Sgr A* (black) and 1E1740.7-2942 (red) are included. The 90% confidence interval ($\Delta\chi^2_{\rm max} - 4.61$) is smaller compared to the single regions in Fig. 19.

also discussed the two sources in a physical context. While Sgr A* is not known to emit in the positron annihiliation range, an apparent detection of a transient spectral feature close to 511 keV during observations with SIGMA was reported for 1E1740.7-2942 (Bouchet et al. [1991] and Gilfanov et al. [1991]), following it to be referred to as the 'Great Annihilator'. Given that no repetition of the phenomenon has been reported, e.g. neither by Jung et al. [1995] and Smith et al. [1996], it was subsequently doubted as a source of a positron annihilation signal. In addition to these observation, Skinner et al. [2014] have also searched for indications in their data of a compact 511 keV source at the position of 1E1740.7-2942 and found none.

For these reasons, we also performed a fit with a point source at the position of 1E1740.7-2942. In contrast to previous data evaluations, we find an emission signal in all energy ranges considered. The oPs flux is $F_{\rm oPs} = (1.8 \pm 0.3)\,10^{-4}\,{\rm ph\,cm^{-2}\,s^{-1}}$, while we determine a flux of $F_{511\,\rm keV} = (8.7 \pm 1.3)\,10^{-5}\,{\rm ph\,cm^{-2}\,s^{-1}}$ for the 511 keV line, both significant at a level of $\sim$6–7σ. The continuum shows the weakest and least significant (2.3σ) signal with a flux of $F_{\rm con} = (6.5 \pm 2.8)\,10^{-5}\,{\rm ph\,cm^{-2}\,s^{-1}}$.

5.2.1 Variability in the Brightness of 1E1740.7-2942

Lightcurves of 1E1740.7-2942 in the X-ray range 14–195 keV (data from the Swift/BAT transient monitor, Krimm et al. [2013], `https://swift.gsfc.nasa.gov/results/bs70mon/SWIFT_J1743.7-2946`) show variabilities in its brightness (Fig. 21).

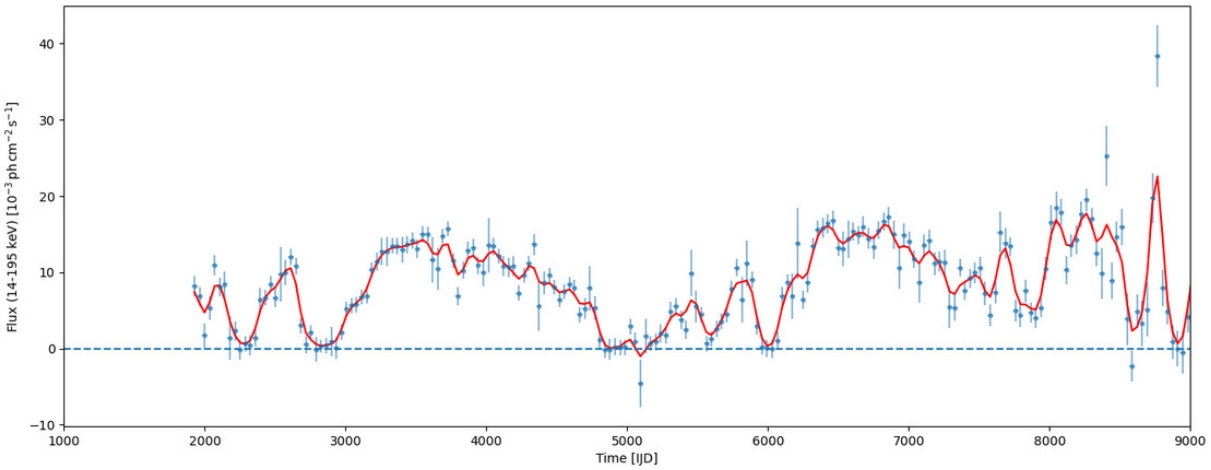

Fig. 21: Lightcurve of 1E1740.7-2942 in the range of 14–195 keV. The data were taken from the Swift/BAT transient monitor [Krimm et al., 2013]. An adjusted curve profile is shown in red. In order to compare the curves on temporal variability scales with our lightcurves in γ-rays, they were plotted for INTEGRAL Julian Days (IJD) 1000–9000. The first determination of the flux by the Swift/BAT transient monitor took place in October 2004 (1927 IJD).

We have also extracted lightcurves from our SPI data. They are shown in Fig. 22. The figure shows the fluxes for the three energy ranges investigated: 400–502, 502–520, and 520–640 keV. The first lightcurve of the oPs bins shows the highest fluxes with typical values around $2 \cdot 10^{-4}\,\mathrm{ph\,cm^{-2}\,s^{-1}}$ with enhanced fluxes for times t$\sim$4000 IJD and t>6000 IJD (highest flux value of $(1.0 \pm 0.2) \cdot 10^{-3}\,\mathrm{ph\,cm^{-2}\,s^{-1}}$ at t=7750 IJD) , which lies in slight agreement with the fluxes from the X-ray range (Fig. 21).
The 511 keV energy bin lightcurve shows typical fluxes around $10^{-4}\,\mathrm{ph\,cm^{-2}\,s^{-1}}$, with slight enhancements at around 4000 IJD < t < 5000 IJD, but lower fluxes for 5000 IJD < t < 6000 IJD, both also showing in the Swift/BAT X-ray data. The highest flux also shows up t=7750 IJD with a value of $(4.4 \pm 1.1) \cdot 10^{-4}\,\mathrm{ph\,cm^{-2}\,s^{-1}}$.
The 520-640 keV bin shows mostly upper limits with no significant emission on average. Despite, there are some significant flux enhancements around t=4000 IJD and t=8000 IJD with the maximum flux also showing up at t=7750 IJD with a value of $(9.9 \pm 2.2) \cdot 10^{-4}\,\mathrm{ph\,cm^{-2}\,s^{-1}}$.
Thus, all of our lightcurves show enhancements in their fluxes around t=4000 IJD and t=8000 IJD, indicating a slight correlation with the Swift/BAT data. Due to the larger uncertainties of the SPI observations, caused by the observed wavelengths being strongly dominated by background noise, the evaluation and interpretation of the data is very challenging, and any statements about the variability of 1E1740.7-2942 can only be indicative. For example, all three lightcurves show very significant emission signals at t=7750 IJD, which does not necessarily point to 1E1740.7-2942 as a strong γ-ray emitter during this period. Rather, this could also indicate background variability and improper modeling of the background.

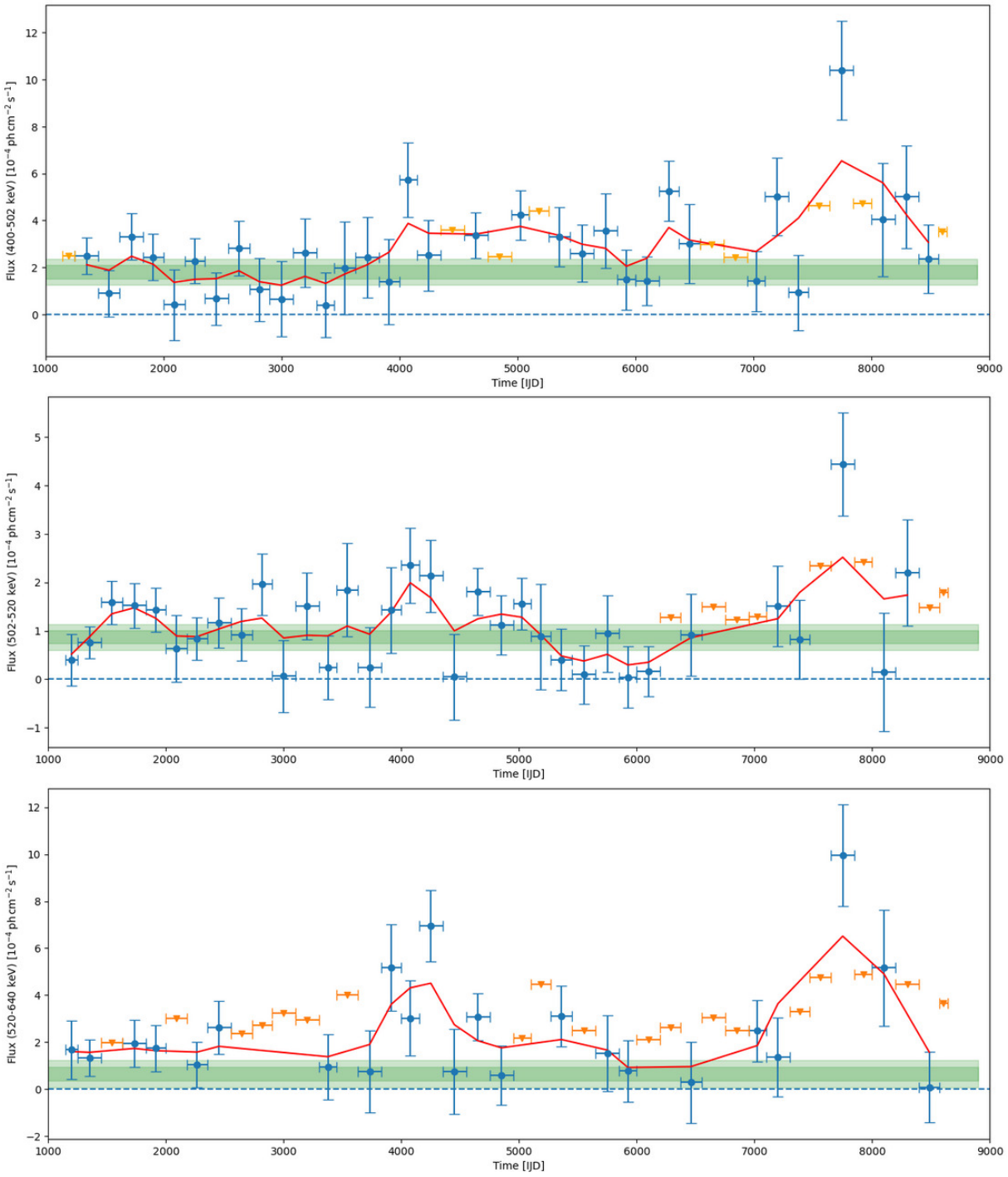

Fig. 22: Lightcurve of 1E1740.7-2942 for the measured γ-ray fluxes (Top: 400-502 keV, Middle: 502-520 keV and Bottom: 520–640 keV). Upper limits are marked with orange triangles. The plots also include the 1σ and 2σ uncertainty bands of the constant fitted fluxes. For comparison, an adjusted curve profile is shown in red similar to Fig. 21.

Nevertheless, it should be noted that, in contrast to previous analyses, 1E1740.7-2942 appears as a significant source in our data. This applies to both a constant and a time-variable fit. Our 20 yr INTEGRAL/SPI dataset, with its much larger database and exposure compared to Skinner et al. [2014], provides the basis for this detection. In this

chapter, both statistical and physical arguments were presented for evaluating 1E1740.7-2942 as not only the hardest X-ray source in the region but also as a γ-ray emitter. Due to the high significance of the signal found, especially for the energy regions 400-502 and 502-520 keV (6-7σ) showing the positron annihilation signal, we decided to include it as an additional point source in our model. This new evidence may warrant a re-evaluation of the 'Great Annihilators' role as a positron annihilation source in the Galactic center region.

6 Extended Source Analysis

In this chapter, we will now focus on extended sources. For this purpose, we will first introduce the various sky model components of the Galactic emission created by Skinner et al. [2014] and Siegert et al. [2016], which serve as the basis for this work. Using these models, we will then extract lightcurves for the bulge and disk from our data in order to find any variability in the Galactic positron annihilation signal. This will be followed by the implementation of the various asteroid populations into our model. The corresponding models and emission templates from Siegert [2024] were presented in Chapter 3. For these, we will also create lightcurves over the INTEGRAL/SPI mission time and then analyze these, in order to find indications for time-variability in their brightness.

6.1 Model Components of the Galactic Emission Signal

The Galactic 511 keV emission signal (Fig. 2) shows a unique structure compared to other wavelengths with very high brightness in the bulge and an extended disk. The bulge requires three components, including a point source, which in the work of Skinner et al. [2014] and Siegert et al. [2016] coincides with the Galactic center, the position of Sgr A* at [ℓ,b] = [-0.06, -0.05]. In Chapter 5, we discussed this point in detail and decided on this component for 1E1740.7-2942. The extended models (the 2D Gaussians narrow bulge NB and broad bulge BB, as well as the disk as elongated 2D Gaussian), in contrast, are taken from the previous works, so that our model now consists of twelve sky components, the continuum point sources mentioned above (Tab. 3) and four additional ones, which can be found in Tab. 4. Here we can see that the NB component also shows asymmetry, with a peak at [ℓ,b] = [-1.25, -0.25]. The resulting general structure of the Galactic positron annihilation signal can also be found using image reconstruction algorithms (e.g., Richardson-Lucy Knödlseder et al. [2005] and Yoneda et al. [2025]), even though image artifacts naturally emerge from the finite number of measured photons.
High-resolution spectroscopy of the 511 keV line for both, the bulge and the disk, suggests that the annihilation of positrons occurs dominantly in the interstellar medium, which would partly explain the 'diffuse' nature of the image [Siegert, 2023].

Component	Lon. [deg]	Lat. [deg]	Lon. extent (FWHM) [deg]	Lat. extent (FWHM) [deg]
NB	-1.25	-0.25	5.75	5.75
BB	0.00	0.00	20.55	20.55
Disk	0.00	0.00	141.29	24.73
1E1740.7-2942	-0.88	-0.11	0.00	0.00

Tab. 4: Sky model components used in our model describing the Galactic positron annihilation signal. Shown are the peak position, as well as the longitudinal and latitudinal extents of the 2D Gaussians describing the different parts [Siegert et al., 2016]. 1E1740.7-2942 is a point source and as such is not extended.

6.2 Lightcurve Extraction

We will now create lightcurves for the bulge and disk in order to investigate the possibility that the "Galactic emission" already shows some changes. Due to the high brightness (especially in the bulge), we are able to do this on a two-year timescale and for both, the oPs energy range of 400-502 keV, as well as also for the narrow 511 keV bin of 508-514 keV. In a later step, after we have also included the asteroids, this model will then serve as a baseline for us to test the variability for the asteroid populations.

The resulting lightcurves of the Galactic bulge and disk can be seen in Fig. 23.
While the flux of the bulge in the 511 keV bin is consistent with a constant flux of $(9.9 \pm 0.5) \cdot 10^{-4}\,\mathrm{ph\,cm^{-2}\,s^{-1}}$, it shows some brightness in the oPs energy bin for 4000 IJD $<$ t $<$ 6000 IJD. The constant flux here is at a value of $(2.3 \pm 0.2) \cdot 10^{-3}\,\mathrm{ph\,cm^{-2}\,s^{-1}}$.
The emission of the disk shows traces of variability in time for both the 511 keV line and the oPs spectrum. For this reason, we have fitted a sinusoidal curve to the lightcurves in addition to a constant curve, which can also be seen in Fig. 23. We find that the variation in the disks' 511 keV bin is consistent with a constant flux of $(14.5 \pm 1.3) \cdot 10^{-4}\,\mathrm{ph\,cm^{-2}\,s^{-1}}$, but also consistent with a period of 16.6 ± 1.5 yr. The constant flux estimated for the oPs energy bin is $(65.1 \pm 7.1) \cdot 10^{-4}\,\mathrm{ph\,cm^{-2}\,s^{-1}}$, but it is also consistent with a variation having a period of 14.0 ± 2.3 yr.
The variations in the disk's emission could be related to the Solar cycle, especially since the timescale of the variations in oPs energy bin of 14.0 ± 2.3 yr is within the range of the Solar activity with its timescale of 11 yr. We have also compared the lightcurves with the measurements of the Solar modulation potential ϕ (Fig. 11). Here we see low ϕ values between IJD 3000 and 4000, a Solar maximum between 5000 IJD and 6000 IJD, followed by decreasing ϕ values and a minimum between 7000 IJD and 8000 IJD. This curve is very similar to the measured fluxes in the disk. Due to its large extent over a large area at the

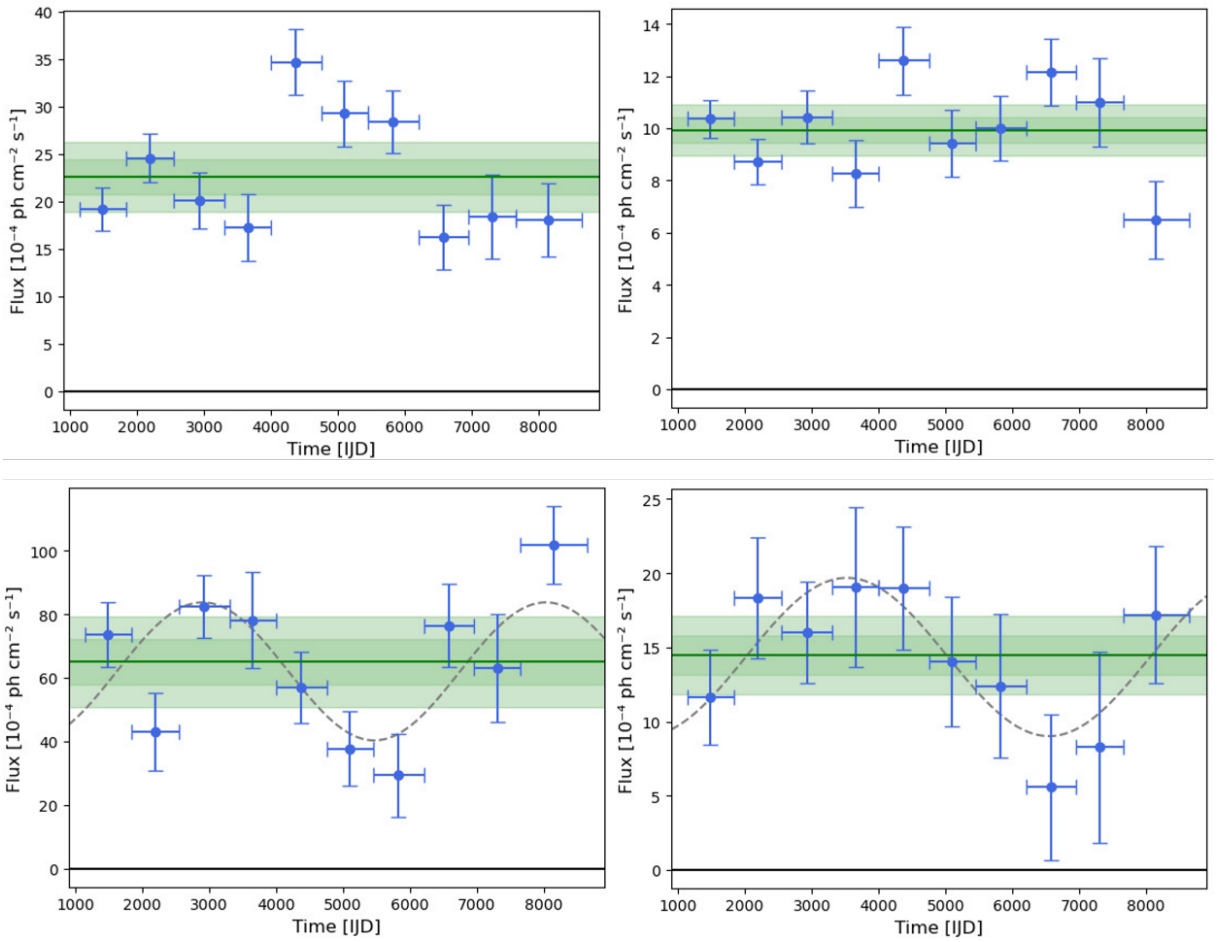

Fig. 23: Lightcurves (blue crosses) for the Galactic bulge (top) and the disk (bottom) to analyse time variability in their oPs signal (left), as well as their 511 keV emission(right). The 511 keV energy bin reaches from 508 to 514 keV, he oPs energy bin from 400 to 502 keV. The green line is a constant fitted to a data indicating also the 1σ (dark) and 2σ (light) uncertainty band. The lightcurves of the disk unclude also a fitted sinusoidal curve (grey).

sky, it also shows the largest overlap with the ecliptic and thus alsso with several asteroid populations. Stronger modulation of Galactic CR reduces positron production and thus also the flux of asteroids (Sec. 3.3). The variabilities observed for the disk could therefore originate from several asteroid populations that are not taken into account in the current model. However, this may also simply be a sign of improper background modeling. In this case, variations in the emission signal also appear on the timescale of Solar activity.

6.3 Sky Models of the Asteroid Populations

To test whether the variability in the positron annihilation signal of the disk in the previous model actually comes from the asteroids, we will now integrate them into our model. We use the previous setup as our baseline to which we add more components. The KBO template (Fig. 8) is static, so that we can add it without changes to the data analysis

method. However, the JT and NT emission templates (Fig. 9) change as a function of time. Actually, an image of JT and NT would have to be created for each pointing. The calculation of these images for the whole sky and the subsequent application of the image response are computationally very complex and would take a very long time. Thus, we model the emission on different subsets of the whole dataset, by combining multiple pointings. This is illustrated in Fig. 24.

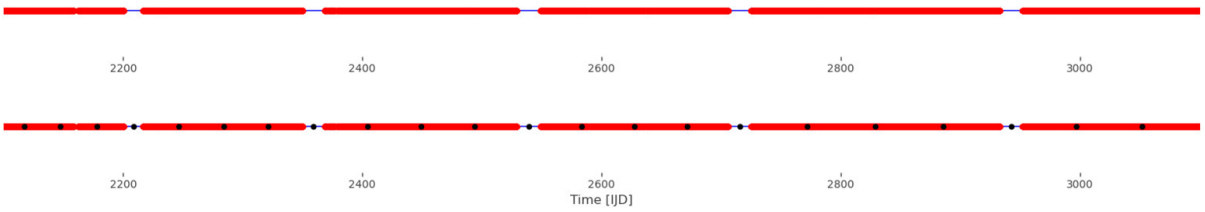

Fig. 24: Timeline illustrating the division of the global dataset into 173 individual sub-datasets with a length of 30-60 days. At the top, each pointing is shown in red, representing the observation periods of INTEGRAL/SPI, which are separated by the annealings (about twice a year, see text). The bottom timeline, in addition, shows the anchor points of the various datasets (black), in which the observation periods are filled evenly.

The observation periods of INTEGRAL/SPI are shown. About twice a year the lattice structure of the SPI germanium detectors are corrected for CR radiation by heating up the camera for several days to ∼100°C. This is called an annealing [Roques et al., 2003]. These annealings naturally separate the observations from each other. These points in time serve as anchor points for splitting the dataset. Further separations are made between two annealing periods. Within one month, the fastest moving objects, the JTs, move only by ∼2.5°, so that this timescale is adequate for further analysis, given the angular resolution of SPI of 2.7°. This results in 173 individual sub-datasets with lengths between 30–60 d to keep observational patterns intact. The bottom timeline in Fig. 24 shows the division of the original dataset.

For each of these sub-datasets, we now create a weighted image for both the JTs and the NTs. To do this, we break down a single dataset d once again — into a dataset d_1 with $p_{1,\max}$ pointings i, each pointing having a start time $t_{i,\,\mathrm{Start}}$, a stop time $t_{i,\,\mathrm{Stop}}$, and the elapse time $t_{i,\,\mathrm{Elapse}}$, and into a dataset d_2 with $p_{2,\max}$ pointings j, respectively. The mean times $t_{1,\,\mathrm{mean}}$ and $t_{2,\,\mathrm{mean}}$ are therefore calculated as follows:

$$t_{1,\,\mathrm{mean}} = \frac{\sum_{i=1}^{p_{1,\max}} \left(t_{i,\,\mathrm{Stop}} - t_{i,\,\mathrm{Start}}\right)/2 \times t_{i,\,\mathrm{Elapse}}}{\sum_{i=1}^{p_{1,\max}} t_{i,\,\mathrm{Elapse}}}$$

$$t_{2,\,\mathrm{mean}} = \frac{\sum_{j=1}^{p_{2,\max}} \left(t_{j,\,\mathrm{Stop}} - t_{j,\,\mathrm{Start}}\right)/2 \times t_{j,\,\mathrm{Elapse}}}{\sum_{j=1}^{p_{2,\max}} t_{j,\,\mathrm{Elapse}}}$$

For both mean times $t_{1,\,\mathrm{mean}}$ and $t_{2,\,\mathrm{mean}}$, images of the asteroid populations im_1 and im_2 are created and then weighted again to generate the final image im_{best} for the respective dataset d.

$$im_{\mathrm{best}} = \frac{\sum_{i=1}^{p_{1,\mathrm{max}}} im_1 \times t_{i,\,\mathrm{Elapse}} + \sum_{j=1}^{p_{2,\mathrm{max}}} im_2 \times t_{j,\,\mathrm{Elapse}}}{\sum_{i=1}^{p_{1,\mathrm{max}}} t_{i,\,\mathrm{Elapse}} + \sum_{j=1}^{p_{2,\mathrm{max}}} t_{j,\,\mathrm{Elapse}}}$$

This approximation allows for quick creation of an image for each of the sub-datasets without having to calculate an image for each pointing. To compare the accuracy, we show this for the first 38 days, i.e. dataset 1. So, the comparative image im_{comp} is

$$im_{\mathrm{comp}} = \frac{\sum_{p=1}^{p_{\mathrm{max}}} t_{p,\,\mathrm{Elapse}} \times im_p}{\sum_{p=1}^{p_{\mathrm{max}}} t_{p,\,\mathrm{Elapse}}}$$

for the images im_p of every potining p.

The comparison between the exactly calculated image and the approximation we used can be seen in Fig. 25. It is clear to see that the deviations are very small ($< 1.5\%$ for the JT, $< 5.5\%$ for the NT), especially at the actual positions of the asteroids. For this reason, the method is well suited for creating the sky model components for the 173 sub-datasets.

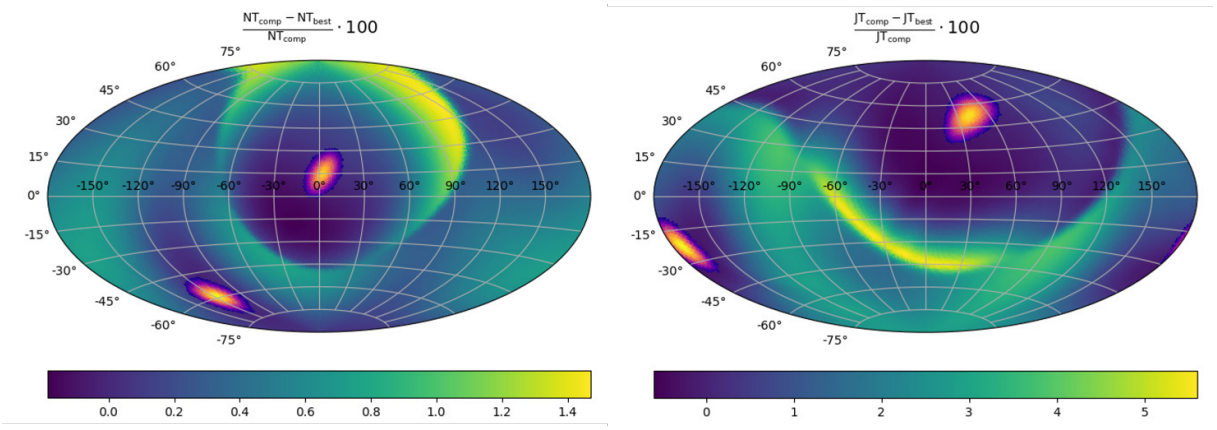

Fig. 25: Comparison of the approximation of our created images (one best image for each dataset) with the comparison image (one image for each pointing) in the case of the first dataset. Deviations are shown as percentages. In addition, sections of the JT and NT are shown in order to evaluate the differences specifically at their position.

According to Eq. 1 in chapter 5, each of these images must now be convolved with the response of the SPI instrument (coded-mask shadowing). Given the size of the dataset, this step is computationally very expensive. Subsequently, for a global fit over the entire observation time of INTEGRAL/SPI, the individual convolutions are recombined into a single file and a final image (im_{fin}) is created from the best images im_{best} of each dataset d for both the JTs and the NTs

$$im_{\mathrm{fin}} = \frac{\sum_{d=1}^{173} t_{d,\,\mathrm{Elapse}} \times im_{\mathrm{best,\,d}}}{\sum_{d=1}^{173} t_{d,\,\mathrm{Elapse}}}$$

by weighting them with the corresponding elapse time $t_{d,\,\mathrm{Elapse}}$ of the sub-dataset d.

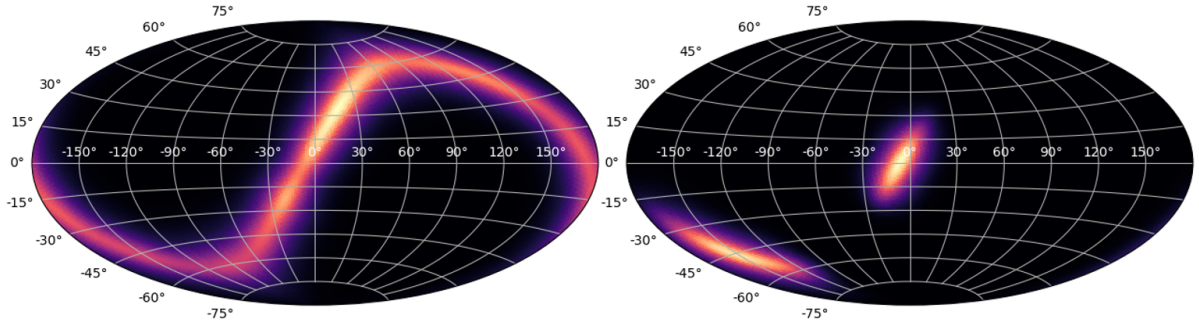

Fig. 26: Final images for JT (left) and NT (right), which will now be integrated as components into our sky model. While the signal from JT accumulated over the INTEGRAL mission period extends across the entire ecliptic, the NT only cover part of the ecliptic, with a bright spot in the Galactic center, due to their long orbit.

The resulting images for the global fit can be seen in Fig. 26. The emission from the JT extends along the entire ecliptic. This is because the dataset covers almost two orbits of Jupiter and its Trojans. A brighter signal can also be seen for positive latitudes. The NT, on the other hand, moves just ∼43.6° over the 20 yr observation period, and its signal thus extends over a much smaller area of the sky.

6.4 Lightcurves of the Asteroids

Having now incorporated the various asteroid populations into our model, we have also extracted lightcurves from the data. These can be seen in Fig. 27. We look at the fluxes again on a 2 yr timescale.

The KBO+MBA constellation shows no significant emission signal during the INTEGRAL/SPI mission time for both, the 511 keV line as well as the oPs. The time-integrated upper limit on the KBO+MBA 511 keV flux is $1.9 \cdot 10^{-3}\,\mathrm{ph\,cm^{-2}\,s^{-1}}$, with typical values per two years of ~ 5 to $30 \cdot 10^{-4}\,\mathrm{ph\,cm^{-2}\,s^{-1}}$. Integrating the upper limits of KBO+MBA between 400 and 502 keV, results in a flux of $6.0 \cdot 10^{-3}\,\mathrm{ph\,cm^{-2}\,s^{-1}}$ given values of ~ 30 to $70 \cdot 10^{-4}\,\mathrm{ph\,cm^{-2}\,s^{-1}}$ on a two year timescale.
The JT also show no significant evidence of positron annihilation. The upper limit is on the order of $\sim 5 \cdot 10^{-4}\,\mathrm{ph\,cm^{-2}\,s^{-1}}$, with typical values per time bin between 0.5 and $15 \cdot 10^{-4}\,\mathrm{ph\,cm^{-2}\,s^{-1}}$ for the 511 keV bin, and, for the oPs energy bin, $\sim 2.5 \cdot 10^{-3}$ $\mathrm{ph\,cm^{-2}\,s^{-1}}$, with typical values per time bin between 20 and $30 \cdot 10^{-4}\,\mathrm{ph\,cm^{-2}\,s^{-1}}$.
On average, the NT show no significant positron annihilation signal, like the KBO+MBA and JT constellations before. In the 400 to 502 keV bin we find an integrated upper limit flux value of $\sim 1.4 \cdot 10^{-3}\,\mathrm{ph\,cm^{-2}\,s^{-1}}$, with typical values per time bin between

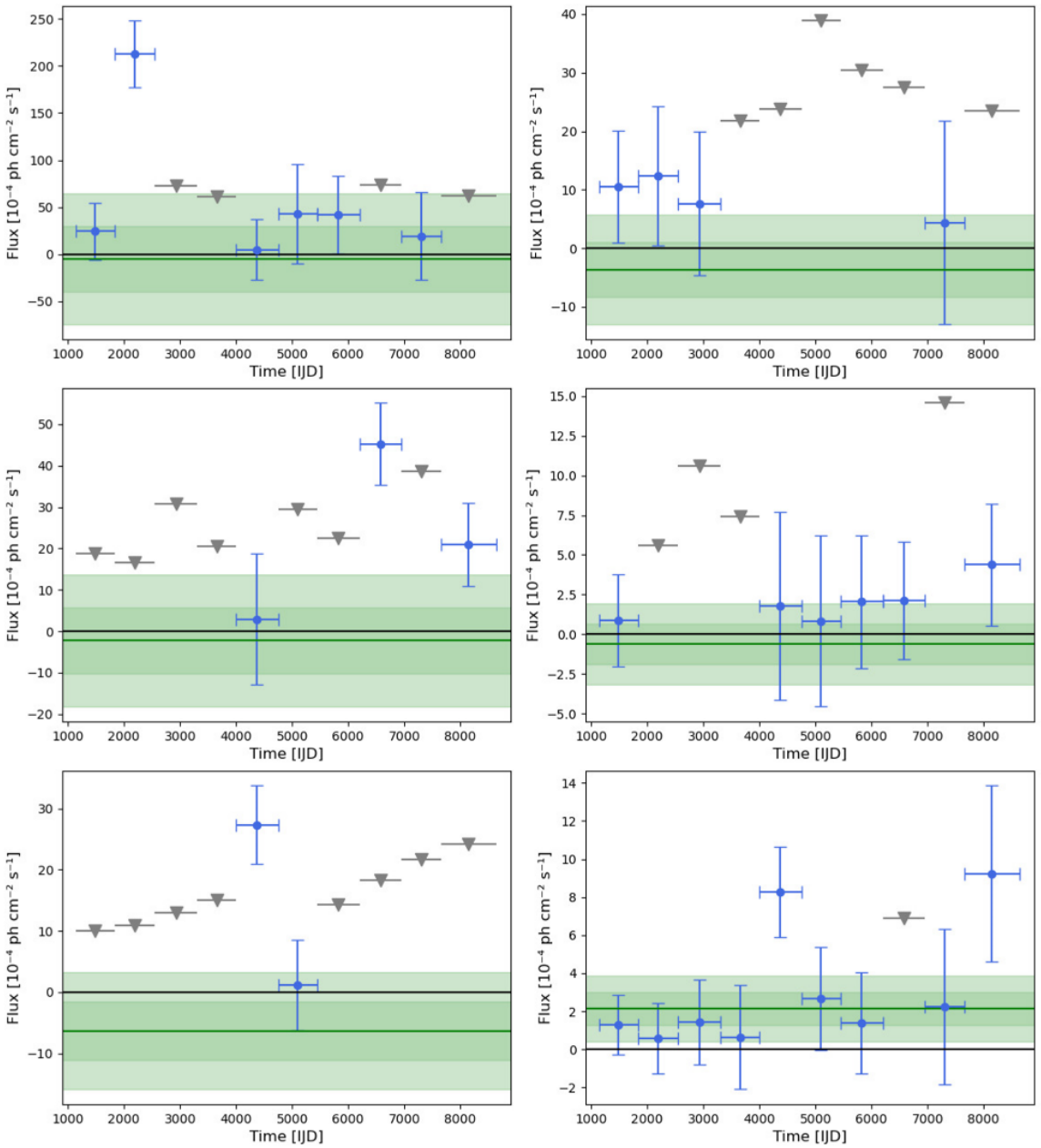

Fig. 27: Lightcurves (blue data points) of the 511 keV energy bin (508–514 keV, right) and oPs energy bin (400-502 keV, left) for the KBO (top), the JT (middle) and the NT (bottom). 2σ upper limits are marked with grey triangles whenever the flux appears to be negative. The green line indicates a fitted constant including 1σ and 2σ uncertainty bands. None of the three asteroid populations shows significant (i.e. $\gtrsim 3\sigma$) emission throughout the 20 yr of SPI observations. The NT component shows two high flux values about 11 yr apart which may point to the Solar cycle.

10 and $25 \cdot 10^{-4}\,\mathrm{ph\,cm^{-2}\,s^{-1}}$. Finally, the 511 keV bin flux is coincident with a value of $2.1 \cdot 10^{-4}\,\mathrm{ph\,cm^{-2}\,s^{-1}}$, showing two enhanced values at t = 4375 and 8145 IJD of $(8.3 \pm 2.4) \cdot 10^{-4}$ and $(9.2 \pm 4.6) \cdot 10^{-4}\,\mathrm{ph\,cm^{-2}\,s^{-1}}$. The data points are 10.3 ± 2.4 yr apart from each other, hinting a tantalizing coincidence in association with the Solar cy-

cle. We can see a flux of $(27.3 \pm 6.4) \cdot 10^{-4}\,\mathrm{ph\,cm^{-2}\,s^{-1}}$ at t = 4375 IJD also for the oPs energy bin. Unfortunately, we see no signal at t = 8145 IJD, the point of the second flux enhancement. We show all flux values and upper limits for all fitted components in Tab. 5.

Component	oPs flux 400-502 keV $[10^{-4}\,\mathrm{ph\,cm^{-2}\,s^{-1}}]$	Positron line flux 508-514 keV $[10^{-4}\,\mathrm{ph\,cm^{-2}\,s^{-1}}]$	HE continuum flux 520-640 keV $[10^{-4}\,\mathrm{ph\,cm^{-2}\,s^{-1}}]$
NB	3.9 ± 1.1	3.5 ± 0.4	2.2 (2σ U.L.)
BB	19 ± 2	6.0 ± 0.7	9.4 ± 2.0
Disk	63 ± 4	14 ± 3	33 ± 4
1E1740.7-2942	1.4 ± 0.4	0.8 ± 0.1	0.7 ± 0.3
Crab	27 ± 4	1.4 ± 0.1	19 ± 4
Cyg-X-1	8.7 ± 0.3	0.2 ± 0.1	5.6 ± 0.3
Cen A	2.3 ± 0.4	0.4 (2σ U.L.)	0.8 ± 0.5
SWIFT J1753.5-0127	2.9 ± 0.4	0.3 (2σ U.L.)	1.7 ± 0.4
GRS 1915+105	0.9 ± 0.3	0.14 ± 0.11	0.9 ± 0.3
MR 2251-178	3.4 (2σ U.L.)	0.9 ± 0.6	3.4 (2σ U.L.)
3C 273	0.9 ± 0.4	0.3 (2σ U.L.)	1.1 ± 0.4
PSR B1509-58	1.0 ± 0.4	0.2 ± 0.1	1.0 ± 0.4
KBO + MBA	60 (2σ U.L.)	19 (2σ U.L.)	55 (2σ U.L.)
JT	25 (2σ U.L.)	5 (2σ U.L.)	23 (2σ U.L.)
NT	14 (2σ U.L.)	2.1 ± 0.9	12 (2σ U.L.)

Tab. 5: All flux values and upper limits for all fitted components and all energy ranges (oPs: 400-502 keV; 511 keV line bin: 508-514 keV and the high-energy (HE) continuum: 520-640 keV).

In order to further test the time variability of the observed NT signal, we used flux expectations (Fig. 11) to create a template with the time binning of our lightcurves that we can now compare with the fit. Fig. 28 shows the extraction of the emission template from the NT expectations (left), as well as its fit to the NT lightcurve of the 511 keV line bin (right).

The observed flux enhancements at t = 4375 and 8145 IJD do not appear as points of notable interest in the expectations. We expect the highest flux at t = 3650 IJD, but find no significant signal there. On the other hand, we expect the weakest fluxes at t > 8000 IJD, where we actually see the highest flux in our fitted lightcurve. Thus, the comparison

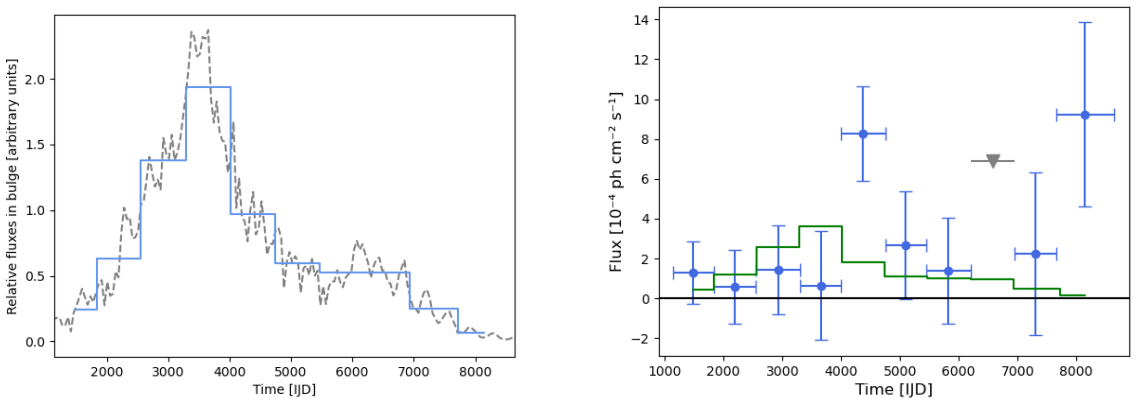

Fig. 28: Comparison of the NT lightcurve with the expectations calculated from the Solar modulation potential (Fig. 11). Left: extraction of an expected emission template with the same time-binning as our fitted lightcurves. Right: fit of the expectation to the actual curve. There is a clear difference between expectation and observation. The strongest signal is expected to appear at t=3650 IJD, at which time we do not see an enhanced flux level. The two enhancements at t= 4375 and 8145 IJD, on the other hand, have no counterpart in the expectation.

with the flux expectations does not suggest any significant correlation. Meaning, that the two high fluxes might be just mere outliers or the result of insufficient background modeling.

In order to better interpret the fit and see how the fitted components correlate or anti-correlate with each other, we have created a correlation matrix for the 511 keV line bin. It can be seen in Fig. 29.
For the sake of clarity and to simplify the comparison, areas have been marked that show the correlation of individual time bins of different components. There are anticorrelations between KBO and JT (green), but also between KBO and NT (yellow). This seems reasonable, since the KBO extends along the entire ecliptic and thus always has points of intersection with the other two asteroid populations. Anticorrelations between JT and NT (blue), on the other hand, are only found at times when they also overlap in the sky. We find examples of this in the time bins 2, 4, 8, and 10. From this, we can calculate a period of 12.1 ± 2.3 yr, coinciding with Jupiter's orbit of 11.86 yr. Due to the two features at the Lagrange points L4 and L5, we see two intersections with a short distance between them. The results of the fits therefore make sense when considering the relative motion of the various asteroid populations in relation to Earth. It can also be seen that there is no significant correlation or anticorrelation between the various asteroids and the Galactic models, which means that the observed fluxes (e.g., enhancements of the NT) were not "taken from" the bulge or disk to the asteroids.

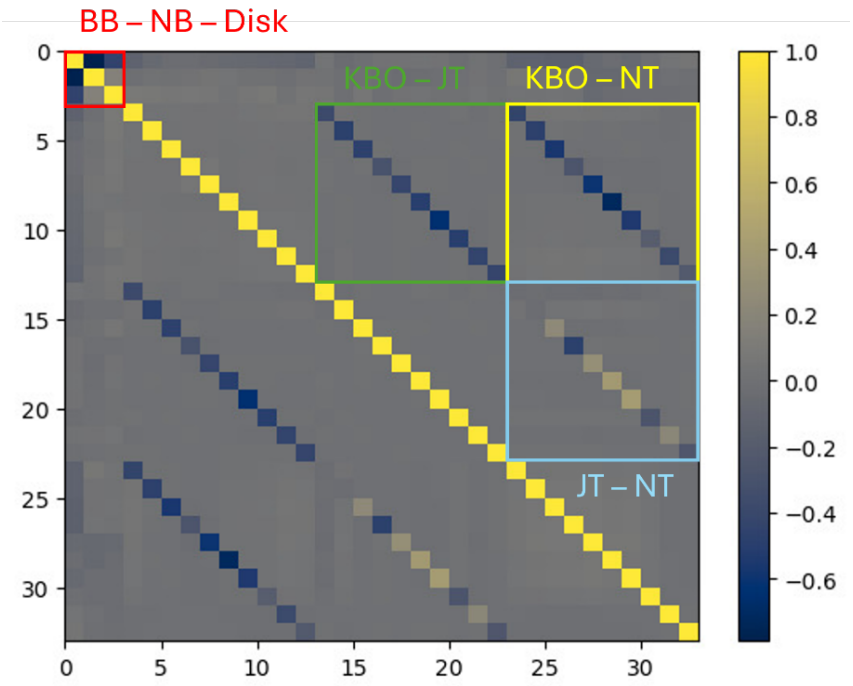

Fig. 29: Correlation matrix for the fitted lightcurves of the 511 keV line of all sky model components. (Anti-)correlations between all fitted time bins are displayed. For simplyfied comparison of the models, areas of interest are framed in color:
Red: Galactic components, Green: KBO - JT correlation, Yellow: KBO -NT correlation, and Blue: JT - NT correlation. In each of the marked areas, the correlation between two components at the same time can be found on the diagonal of the matrix.

As a final test, we analyzed our sky model images of the asteroids in terms of statistical biases. As already briefly explained in Sec. 4.2, our approach and the fitting with `spimodfit` involves a bias, an expectation, that is transferred into the model via the images of the various sky model components even before the fit is performed. Since the background in the MeV-range is very dominant, weaknesses in the modeling can then lead to increased fluxes in the sky components. In the case of very weak signals, or in the most extreme case, if there is no source at all at the assumed position, this can lead to false detections via the statistical bias. To illustrate its role in SPI data analysis, we flipped all asteroid models along Galactic latitude ($\ell = 0°$) and performed another fit. The point sources and Galactic components remain the same in order to make the best possible comparison. The resulting lightcurves are shown in Fig. 30.

We find much higher fluxes compared to Fig. 27 with fewer upper limits, both for the KBO+MBA constellation and for the JT. The KBO shows a 511 keV line flux of $(1.5 \pm 0.4) \cdot 10^{-3}\,\mathrm{ph\,cm^{-2}\,s^{-1}}$ and a flux value of $(8.3 \pm 0.1) \cdot 10^{-3}\,\mathrm{ph\,cm^{-2}\,s^{-1}}$ for the oPs spectrum, with high significance of 3.8σ for the 511 keV line and 83σ for the oPs continuum. These fluxes alone are well above the expectations of Moskalenko et al. [2008], according to which the total positron annihilation signal from MBA+JT+NT+KBO is in

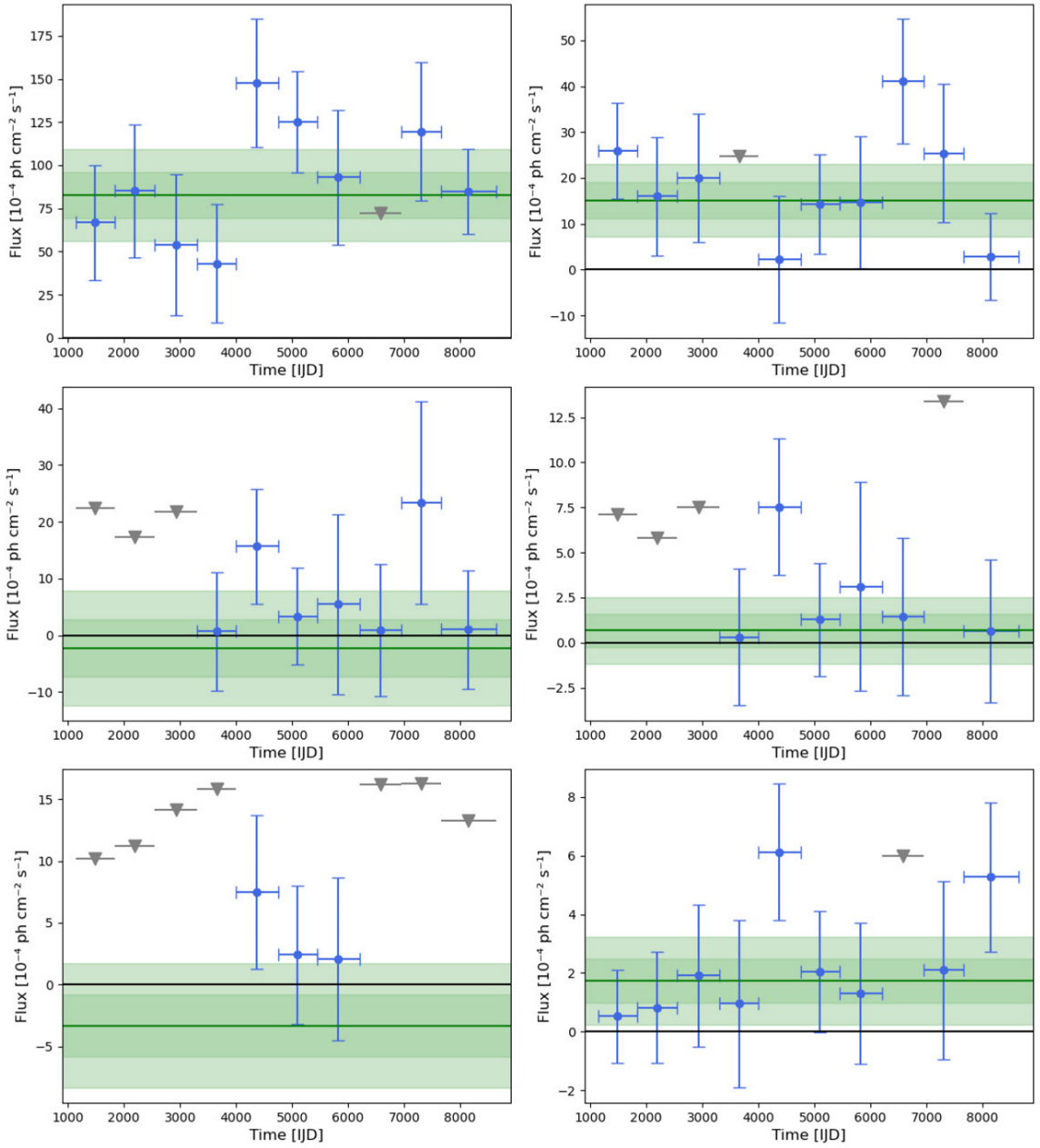

Fig. 30: Lightcurves (blue data points) of the 511 keV energy bin (508–514 keV, right) and oPs energy bin (400-502 keV, left) for the KBO (top), the JT (middle) and the NT (bottom) with the flipped models. 2σ upper limits are marked with grey triangles whenever the flux appears to be negative. The green line indicates a fitted constant including 1σ and 2σ uncertainty bands. The higher fluxes, compared to the original models (Fig. 27), appear due to the statistical bias.

the order of $\sim 5 \cdot 10^{-4}\,\mathrm{ph\,cm^{-2}\,s^{-1}}$. If these results are interpreted incorrectly, they could lead to a wrong detection, at least of the KBOs, since large parts of the image fitted here do not overlap with an actual source. The lightcurves of the NT are most similar to the flipped variant. Due to their long orbital period (Tab. 2) they move significantly slower with respect to Earth, and at the time of observation, this source shows particularly strong

emission in the vicinity of the Galactic center (Fig. 26), which is why the images overlap at this bright spot despite the flip. The second feature of the NT, on the other hand, is located at latitudes between ~ 30 and $60°$ during the observational period, with much less exposure. However, the similarity to the lightcurves of the correct positions might also indicate, that these already show a certain statistical bias. In conclusion, the results of the unflipped sky models provide more evidence in terms of upper limits and significance, especially in the case of the KBOs.

At the end of our analysis, we conclude that we have not found a significant positron annihilation signal for any of the relevant asteroid populations within our Solar System. Observations with future telescopes of higher sensitivity (such as the accepted NASA SMEX mission COSI (Compton Spectrometer and Imager, Tomsick et al. [2019]), which is accepted to launch in 2027) are needed to analyse this time-variable signal. The models, providing flux estimates, use the spatial distribution of different asteroid populations, as well as the response of SSSBs of different sizes. These models should also be further developed to further constrain flux estimates and variability scales. We will address this in the next chapter (Chp. 7) of this thesis and make an early small contribution to this process.

7 Estmating the Solar System γ-ray Albedo

In this chapter, we look at the models and simulations that form the theoretical basis for the γ-ray albedo of SSSBs. Besides Moskalenko and Porter [2008] and Moskalenko et al. [2008], De Gaetano et al. [2023] has also worked on this topic. They simulated the interaction of CRs with asteroids of different sizes using the `FLUKA` code. Their results deviate by 2–6 orders of magnitude from the simulations of Moskalenko et al. [2008] in the GeV range. For this reason, in addition to evaluating SPI data, we have also re-examined the topic from a theoretical perspective and thus performed own simulations using the `GEANT4` framework, as Moskalenko and Porter [2008] did previously. The setup used is shown in Fig. 31.

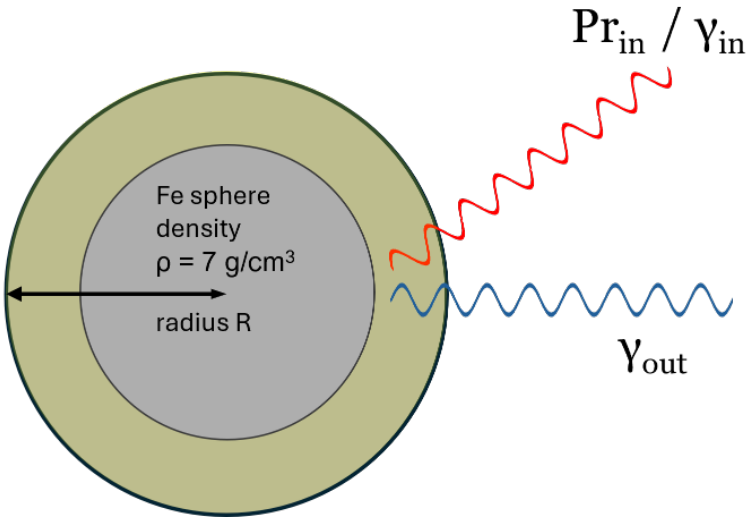

Fig. 31: Setup for our `GEANT4` simulations. A flat spectrum of protons/photons hits an iron sphere with radius R and a density ρ of 7 g/cm^3. The interactions between particles and material take place in the rim marked in yellow.

We shoot a flat spectrum for both cases, photons γ_{in} and protons Pr_{in}, onto an iron sphere (radius R) with a density of $\rho = 7\,\text{g/cm}^3$. The resulting interactions mainly take place within the rim highlighted in yellow. All hadronic and electromagnetic processes within the sphere are taken into account and all photons leaving γ_{out} it are recorded. Differently sized asteroids are simulated in this way and, given their respective responses (photons that escape from the asteroid) and the size distribution of SSSBs in a certain asteroid

population, we compiled the resulting flux as observed from the Earth albedo based on the method of De Gaetano et al. [2023].

The response of an asteroid depends on the type of particles that hit it, i.e., protons or photons, as well as on its size. Since we expect that above a certain asteroid size, the particles can no further enter the interior of the sphere, and for this reason the interactions mainly take place within the rim of an asteroid, the response should not change above a certain simulated size. We will test this and try to make an estimate on the penetration depth/thickness of the rim.

7.1 Photon Interactions

We start with photon interactions. Since we want to calculate the signal from asteroids in the MeV range, we shoot a shower of 10 million photons of a flat spectrum between 10 keV and 100 MeV onto the asteroid spheres of radii R between 0.1 cm and 100 km. The response for selected sizes can be seen in Fig. 32.

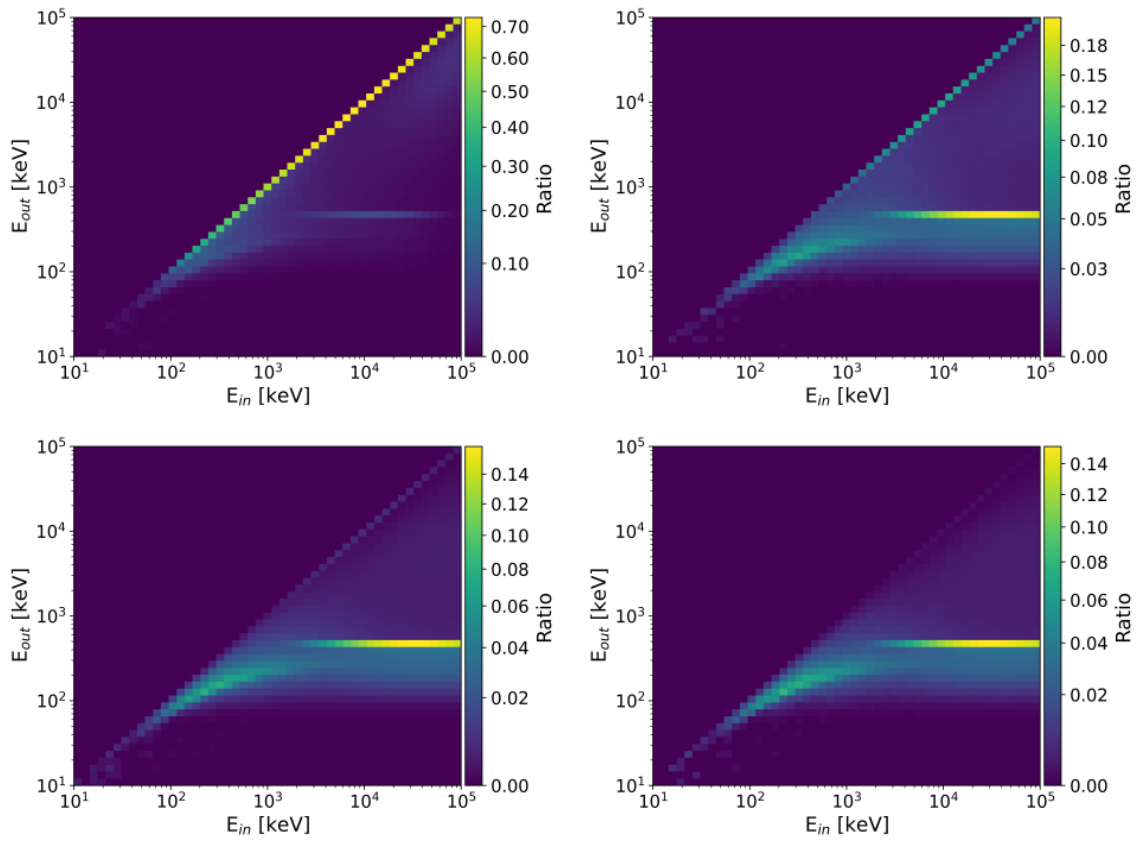

Fig. 32: Response matrices of photon interactions for sphere radii of 1 cm (top left), 10 cm (top right), 50 cm (bottom left), and 100 cm (bottom right). For small radii, the photons often penetrate the material without interacting. For larger sizes, a 511 keV line appears.

For the small SSSBs radii (1 cm), we see that most photons pass through the bodies

without interacting with their material. However, this changes as the radius increases. For a SSSB size of 10 cm, we already see a strongly pronounced 511 keV feedback, and in addition also a clearly visible Compton edge, as these represent the main interaction processes. The comparison between a radius of 50 and 100 cm suggests that the response of the asteroid is almost identical. Beyond a radius of 100 cm, we observe no further changes. It follows that the rim, i.e., the area within which all the processes take place, is approximately 50 cm.

7.2 Proton Interactions

The same procedure was also carried out for proton interactions. A flat spectrum ranging from 10 MeV to 10 GeV was shot at the spheres. Computationally, the simulations were significantly more complex, which is why only sizes from 0.1 cm to 1000 cm were simulated this time. For the same reason, the number of simulated particles is also smaller. For sizes from 0.1 to 30 cm, there were 1,000,000, while for larger sized spheres we had to reduce this to 100,000. We will now again look at the response matrices of different sizes (Fig. 33).

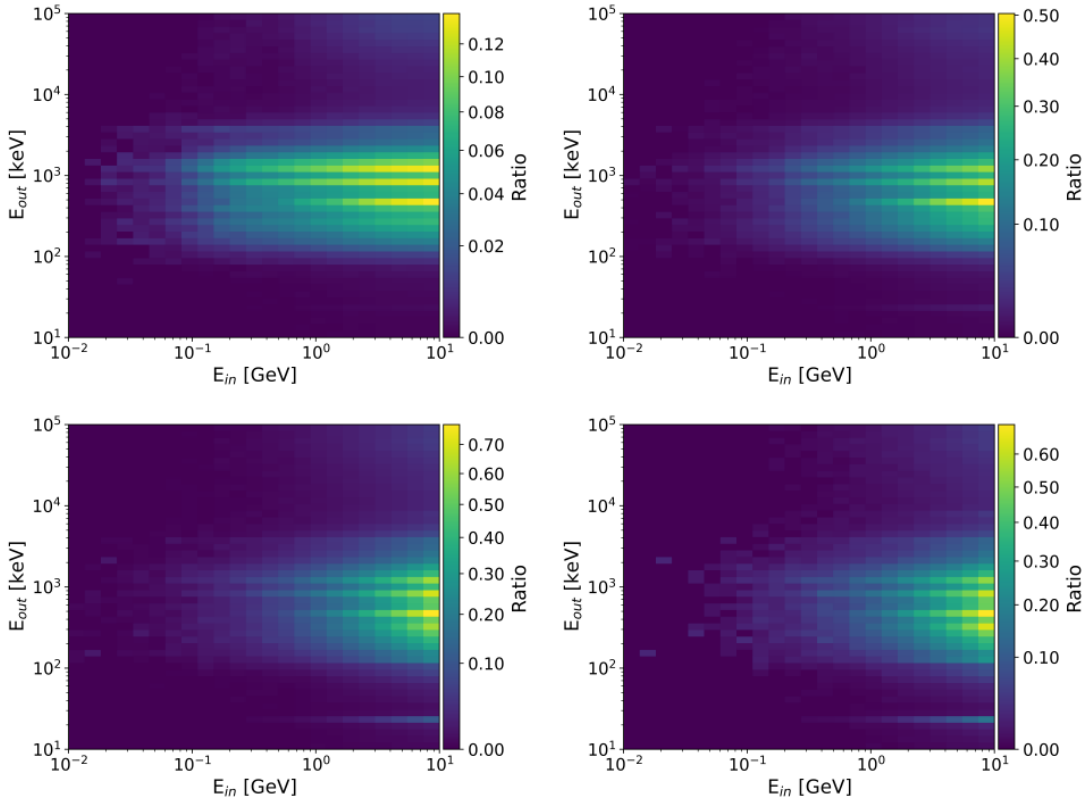

Fig. 33: Response matrices of proton interactions for sphere radii of 1 cm (top left), 10 cm (top right), 50 cm (bottom left), and 100 cm (bottom right). In addition to the 511 keV line, we also observe nuclear iron lines at 0.847 and 1.238 MeV.

Here, in addition to the 511 keV line, two strongest iron lines are clearly visible at 0.847 and 1.238 MeV. The results are similar to those for photon interactions in terms of size dependency. We again observe only minor changes between radii of 50 and 100 cm. Beyond sizes of 100 cm, no significant changes in response can be identified anymore. Overall, the matrices appear grainier (especially beyond radii of 50 cm) this time. This is due to the lower number of simulated particles. Nevertheless, the results are conclusive and thus can be used for further calculations. Simulations with a larger database will follow this work in order to strengthen significance of the results even further.

7.3 Flux Expectations

After generating the responses for selected asteroid sizes, we interpolated between them and now have responses $\mathbf{R}_{\gamma,\,\mathbf{ph}}(\mathrm{r})$ and $\mathbf{R}_{\gamma,\,\mathbf{pr}}(\mathrm{r})$ for every size between 0.1 and 100,000 cm. To calculate the flux expectation on Earth from this, we first look at the number density dN/dr of SSSBs within a certain asteroid population. It is given by a simple powerlaw (De Gaetano et al. [2023] and Dohnanyi [1969])

$$\frac{\mathrm{dN}}{\mathrm{dr}} \;=\; \mathrm{a} \cdot \mathrm{r}^{-\alpha} \tag{9}$$

with

$$\mathrm{a} \;=\; \frac{3\,\mathrm{M}}{4\,\pi\,\rho} \times \frac{4 \,-\, \alpha}{\mathrm{r}_1^{4-\alpha} \,-\, \mathrm{r}_0^{4-\alpha}}$$

for $\alpha \neq 4$. Given the total mass M and the smallest and largest radius (r_0 and r_1) of a certain asteroid population, as well as the density ρ of the bodies included, we can use this to calculate their number distribution. The flux on Earth $\mathrm{F}_{\mathrm{Earth}}(E)$ can now be calculated from the flux f(E, r) of an r-sized asteroid at the production site.

$$\mathrm{f(E,\,r)} \;=\; \mathbf{R}_{\gamma}(\mathrm{r})\,\mathrm{S_{in}(E)} \tag{10}$$

$\mathrm{S_{in}}$ is the input spectrum, meaning the CR spectrum for our case. Moskalenko et al. [2008] and De Gaetano et al. [2023] use two slightly different approaches, which nevertheless explain the large difference between their calculated fluxes. According to De Gaetano et al. [2023] the flux on Earth is given by

$$\mathrm{F_{Earth}(E)} \;=\; \int_{\mathrm{r_0}}^{\mathrm{r_1}} \frac{\pi\,\mathrm{r}^2}{\mathrm{d}^2}\,\mathrm{f(E,\,r)}\,\frac{\mathrm{dN}}{\mathrm{dr}}\,\mathrm{dr} \tag{11}$$

including the albedo of an asteroid population with distance d to the Earth including SSSBs of sizes r between r_0 (min) and r_1 (max) with the flux f(E, r) at the production site. The parameter α is contained in the number distribution dN/dr and also depends on the considered asteroid population. Moskalenko et al. [2008] were using a different

approach. They have just one assumed emission template of a Moon-sized body $F_{Moon}(E)$ which they normalise by the parameters of the Moon and scale it down to smaller sized SSSBs

$$F_{Earth}(E) \;=\; F_{Moon}(E)\,\frac{D_{Moon}^2}{d^2}\,\int_{r_0}^{r_1}\frac{dN}{dr}\,\frac{r}{R_{Moon}}\,dr \tag{12}$$

with D_{Moon} being the distance between the Moon and the Earth and R_{Moon} being the Moon's radius.

The two different approaches reveal the large deviations in the results obtained from the models. Moskalenko et al. [2008] uses only one emission template [Moskalenko and Porter, 2008]. However, due to their significantly larger number, the smaller bodies contribute much more to the overall signal of all the asteroid populations, which is why the more complex simulations of De Gaetano et al. [2023] differ in this point and take the effect of the complex shapes into account more accurately. In addition, Moskalenko et al. [2008] use a different dependency with r^1 on the size of the SSSBs themselves, where De Gaetano et al. [2023] include a dependency of r^2 in their calculations. Since Moskalenko et al. [2008] normalize the radii to scales of the Moon, the term $\frac{r}{R_{Moon}}$ yields higher fluxes when it is inserted into the equation linearly rather than squared. In their scaling, De Gaetano et al. [2023] refer to the surface of the respective asteroid as the origin of the signal ($A = \pi r^2$). Due to our advanced model, which also includes different body sizes, we have opted for their approach, but also take into account the influence of the rim within which most particle interactions take place.

Given the size of the rim Δ, we have a luminous sectional area A of

$$A \;=\; \pi(r^2 - (r-\Delta)^2) \;=\; 2\,\pi\,r\,\Delta \;-\; \pi\,\Delta^2 \tag{13}$$

We use this expression for A in the case of $r > \Delta$. For the smallest bodies ($r < \Delta$), however, we use the description by De Gaetano et al. [2023] as an approximation. Our adapted calculation of the flux is then given by

$$F_{Earth}(E) \;=\; \int_{r_0}^{r_1}\frac{A}{d^2}\,f(E,\,r)\,\frac{dN}{dr}\,dr \tag{14}$$

with

$$\begin{aligned} A &= 2\pi r\Delta - \pi\Delta^2 && \text{for } r > \Delta \\ A &= \pi r^2 && \text{for } r \leq \Delta \end{aligned}$$

With all this taken into consideration, we can now calculate the flux expectations at the position of Earth from our simulated responses and the interpolations for the radii in-between. As an example, we will focus on the MBA asteroid population, which also served as the basis for the calculations of De Gaetano et al. [2023]. Here, the total mass

of the population is M $= 5 \cdot 10^{-4}\,\mathrm{M}_{\oplus}$ and the distance to Earth is d=2.7 AU. The power law index α=–2.7 for the size distribution dN/dr of the bodies.
We use the BAT CXB spectrum as the input spectrum for the CR photons [Ajello et al., 2008].

$$\frac{\mathrm{dN}}{\mathrm{dE}_{\mathrm{ph}}} = \frac{10.15 \cdot 10^{-2}}{(\mathrm{E}/29.99)^{1.32} + (\mathrm{E}/29.99)^{2.88}}\ \mathrm{keV}^2\,\mathrm{ph\,cm}^{-2}\,\mathrm{s}^{-1}\,\mathrm{sr}^{-1}\,\mathrm{keV}^{-1} \tag{15}$$

In the case of proton interactions, the input CR spectrum from Moskalenko and Porter [2008] is used.

$$\begin{aligned}\frac{\mathrm{dN}}{\mathrm{dE}_{\mathrm{pr}}} = 1.6 \cdot 10^4 \Big(&(E + 0.458)^{2.75} - 3.567\,(E + 0.936)^{-4.90} \\ &+ 4.777 \cdot 10^5\,(E + 14.4)^{-6.88} \Big)\ \mathrm{nucleon\,m}^{-2}\,\mathrm{s}^{-1}\,\mathrm{sr}^{-1}\,\mathrm{GeV}^{-1}\end{aligned} \tag{16}$$

The resulting γ-ray signal for the MBA is shown in Fig. 34.

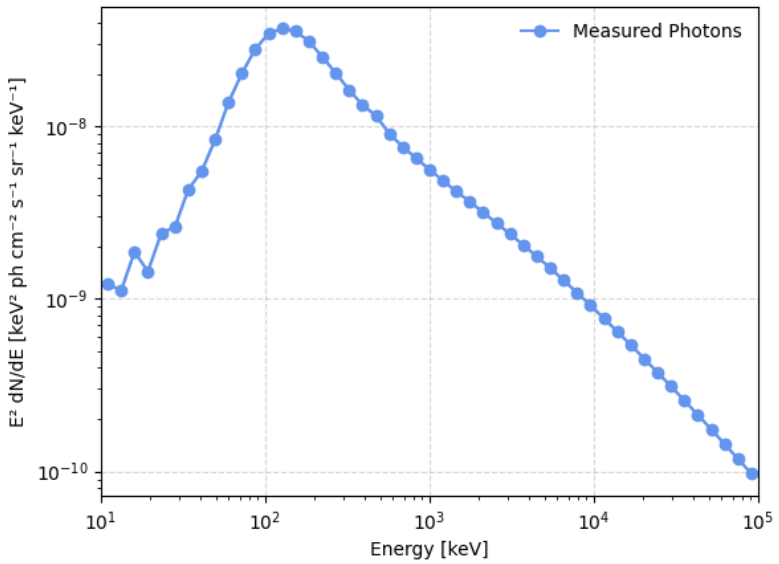

Fig. 34: Calculated observable spectrum on Earth, resulting from the interaction of CR photons with the MBA. The resulting signal shows very small fluxes with a peak at approximately 100 keV. The 511 keV line, which was clearly visible in the response matrices (Fig. 32), can hardly be seen in the spectrum.

We see a very weak signal, peaking around 100 keV with a flux of $\sim 4 \cdot 10^{-8}\,\mathrm{keV}^2\,\mathrm{ph\,cm}^{-2}\,\mathrm{s}^{-1}\,\mathrm{sr}^{-1}\,\mathrm{keV}^{-1}$. The spectrum shows no enhanced 511 keV emission. This would require high-energy photons. The peak of the cosmic γ-ray background (CGB) is ~20 keV. Photons with an energy of 1 MeV, on the other hand, occur two orders of magnitude less frequent.

The spectrum for proton interactions can be seen in Fig. 35. Here, we compare our results

with those of De Gaetano et al. [2023]. In order to compare the fluxes, we converted our results into the same units.

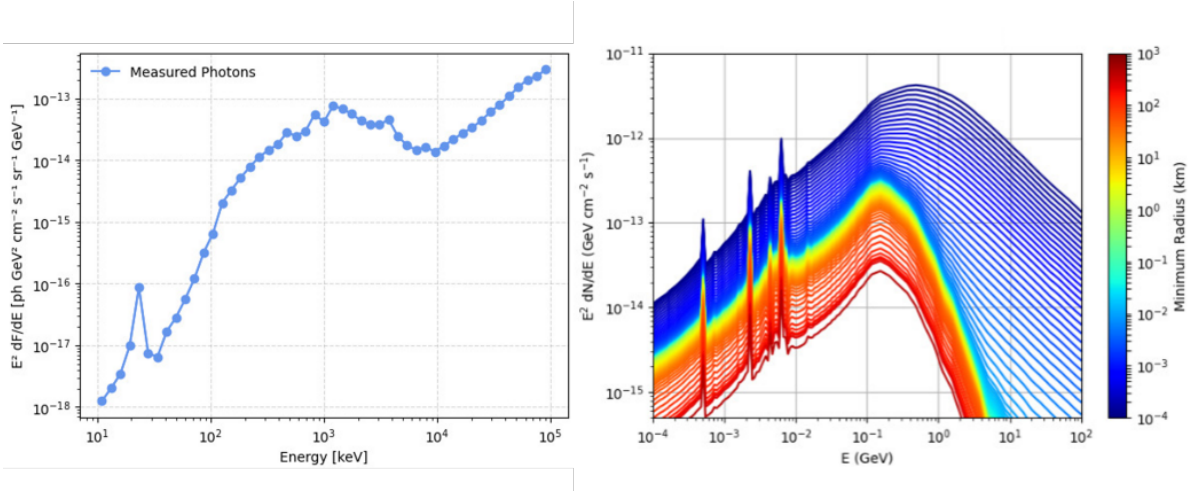

Fig. 35: Calculated observable spectrum on Earth, originating from the proton interaction of CRs with the MBA (left), as well as the calculated spectra (right) for ice spheres by De Gaetano et al. [2023] for different threshold sizes of SSSBs (coded by their respective color). For comparison, we use the dark blue curve (smallest radius 10^{-4} km, in our case: 10^{-6} km). The results are highly consistent with each other. Both show a dip at ~ 8 MeV and differ by a maximum of one order of magnitude. However, the nuclear lines are more pronounced in the spectra of De Gaetano et al. [2023] due to a narrower binning.

A comparison reveals a strong agreement between our results and the previous calculations of De Gaetano et al. [2023], despite the use of different frameworks (`FLUKA` and `GEANT4`). They illustrated several spectra for different asteroid population compositions, with the respective color coding the smallest bodies in each case. For our comparison, we use the dark blue spectrum with the highest fluxes, which uses 10^{-4} km as the threshold for the SSSB size. In our case, the smallest radius of an object is 10^{-6} km. The spectrum shows a slight dip at ~ 8 MeV, which we also observe in the spectra of De Gaetano et al. [2023]. The largest deviations are visible at ~ 100 MeV, the upper bound of our spectrum, with around one order of magnitude. However, given the generally very small fluxes of $\sim 10^{-17} - 10^{-12}\,\mathrm{GeV^2\,ph\,cm^{-2}s^{-1}\,sr^{-1}\,GeV^{-1}}$, this is not of particular importance. Differences between the plots can be seen in the nuclear lines, which are much more pronounced in the emission spectra of De Gaetano et al. [2023]. The sphere simulated by them consisted of ice and had a density of $1\,\mathrm{g/cm^3}$. In addition, they performed their simulations with carbon and silica, using also different densities.

The work on the calculation of our expectations is still ongoing. We will perform further simulations with different compositions of the spheres, different densities and also larger samples (especially for the interactions with protons, helium, electrons and positrons). But, these preliminary results already indicate, especially in their agreement with De Gaetano et al. [2023], that the Solar System γ-ray foreground might be several orders of

magnitude smaller than calculated by Moskalenko et al. [2008].
It should also be mentioned that they used different parameters for the asteroid populations in their calculations. They accumulate the γ-ray albedo of bodies of all populations and therefore used a power law index $\alpha = -3.5$. This leads to a significantly steeper profile of the size distribution dN/dr of the SSSBs and, at the lower end, to a large number of additional objects compared to our calculations and those of De Gaetano et al. [2023]. However, this additional discrepancy between the models does not result in the largest deviations. The main differences between the various approaches are related to the respective scaling when converting local fluxes (or yields) of different-shaped objects into actually observable fluxes at Earth.

8 Discussions

8.1 Origin of the Offset in the Galactic Center

We started our analysis with an investigation of the sky model components used in this work. We found an offset of the 511 keV emission in the Galactic center, also observed for the 10 yr INTEGRAL/SPI dataset by Skinner et al. [2014]. The two possible emitters of the positron annihilation signal in this location, Sgr A* and 1E1740.7-2942, as well as different statistical and physical arguments, have been presented. In contrast to previous observations, we find a significant emission signal at the position of 1E1740.7-2942 and could also extract lightcurves for our data. This, after several non-detections following the SIGMA observation from 1991, might bring back the discussion about 1E1740.7-2942 as a 511 keV emitter and perhaps not label the expression 'Great Annihilator' as misleading anymore.
Nevertheless, it remains to be said that this is not absolute evidence for 1E1740.7-2942 as the origin of the Galactic offset. Therefore we would need 1E1740.7-2942 to be also observed in a follow-up mission, which is very hard due to the small fluxes observed in our dataset. Regardless of that, the Galactic center, as showing the brightest 511 keV signal, has to be observed continuously and also further improvements of the models should be made in order to be able to close this debate.

8.2 Solar System γ-ray foreground

We investigated whether various predictions and estimates of the 511 keV foreground of several asteroid populations can actually be found in the data of INTEGRAL/SPI using a dataset of 20 yr. Except for two flux enhancements on the order of $2-3\,\sigma$ for the NT, we found no significant emission. These do not coincide with expectations calculated from the Solar modulation potential and thus both data points may be mere outliers. However, given these expected fluxes from theoretical studies, the signals of all asteroid populations should be investigated further. Given the estimates of Moskalenko et al. [2008], the total 511 keV flux along the ecliptic (KBO+MBA+JT+NT) could be on the order of $\sim 5 \cdot 10^{-4}\,\mathrm{ph\,cm^{-2}\,s^{-1}}$. Our individual fluxes for the asteroid families are consistent with this flux level, except for the KBO+MBA case in which our upper limits are about a factor of 4–5 higher than the total expectation. Observations with future telescopes of higher

sensitivity are needed to analyse this time-variable signal. The models used, such as the spatial distribution of different asteroid populations, as well as the response of SSSBs of different sizes, should also be further developed to further constrain flux estimates and variability scales.

Moskalenko et al. [2008] use the emission template of the Moon and scale it down various asteroid sizes to calculate the γ-ray albedo of SSSBs of all asteroid populations, by using a linear dependency on the radius. De Gaetano et al. [2023] used a different approach, where they scale the different sizes with their surface as luminous area. Their results deviate by 2–6 orders of magnitude from the simulations of Moskalenko et al. [2008] in the GeV range. We performed own simulations to also obtain results in the soft (MeV scales) γ-rays. During this process we developed an additional method, by not only considering the surface of the bodies as luminous area, but instead focus on the rim, within which most of the particle interactions take place.

Indeed, our calculations are in strong agreement with the estimates of De Gaetano et al. [2023] with resulting flux estimates that are several orders of magnitude smaller, compared to Moskalenko et al. [2008] and also compared to our fit results for all asteroid populations (see Tab. 5). If those were correct, there is hardly any chance to observe these emission features even with next generation telescopes.

Our analysis made use of all INTEGRAL/SPI observations from 2003-2023 for which most observations are concentrated in the Galactic bulge and disk. There is certainly a bias in the observations far from high latitudes and especially the ecliptic. With a wide field of view imager, such as COSI [Tomsick et al., 2019], these observational constraints could be alleviated, so that highly accurate and sensitive measurements also on shorter timescales will be possible. COSI will have a sensitivity to the entire sky within 2 yr of $1 \cdot 10^{-5}$ph cm^{-2} s^{-1} at 511 keV, so that the predictions by Moskalenko et al. [2008] could be firmly excluded

9 Conclusion

In this thesis, we investigated various manifestations of temporal variations in the Galactic positron annihilation signal. We initially focused on the Galactic center, the brightest source of the emission. Here, we found an offset in the observed signal, which had already been detected in previous studies using smaller datasets from INTEGRAL/SPI. Two possible emitters that could cause the offset are Sgr A*, the supermassive black hole at the center of the Milky Way, and 1E1740.7-2942, a microquasar and the strongest source of X-rays in this region. Statistical arguments can be found for both sources. However, 1E1740.7-2942 was already considered a potential 511 keV emitter and was labeled the 'Great Annihilator' after signals were observed near the positron annihilation line with SIGMA in 1991. However, various follow-up observations could not find a significant γ-ray signal at its position. We have now found further evidence of 1E1740.7-2942 in our data and have even been able to extract lightcurves from our data. When comparing these with lightcurves from the X-rays, we also found indications of similarities. This motivated us to include 1E1740.7-2942 in our model, in contrast to Sgr A* in previous work.
In the main part of this work, we investigated whether various estimates and predictions of the Solar System γ-ray foreground can be found our dataset. Therefore, we examined various asteroid populations within the Solar System. We found no significant evidence for any of them. According to our results, the positive latitude enhancement observed in previous analyses [Purcell et al., 1997] and reffered to as 'OSSE-fountain' cannot have been caused by the JT and NT. For this reason, we have simulated the interactions of CRs with SSSBs of different sizes. In addition to Moskalenko et al. [2008], De Gaetano et al. [2023] have also performed calculations of the Solar System γ-ray foreground. Our theoretical models provide a new scaling between the asteroid sizes, which refers to the rim, within which most of the particle interactions take place. The strong coincidence between our calculations and those of De Gaetano et al. [2023], with differences of 2–6 orders of magnitude from Moskalenko et al. [2008], suggests that the Solar System γ-ray foreground is significantly weaker than previously assumed.

Bibliography

M. Ajello, J. Greiner, G. Sato, D. R. Willis, G. Kanbach, A. W. Strong, R. Diehl, G. Hasinger, N. Gehrels, C. B. Markwardt, and J. Tueller. Cosmic X-Ray Background and Earth Albedo Spectra with Swift BAT. , 689(2):666–677, December 2008. doi: 10.1086/592595.

H. Akaike. A New Look at the Statistical Model Identification. *IEEE Transactions on Automatic Control*, 19:716–723, January 1974.

W. B. Atwood, A. A. Abdo, M. Ackermann, W. Althouse, B. Anderson, M. Axelsson, L. Baldini, J. Ballet, D. L. Band, G. Barbiellini, J. Bartelt, D. Bastieri, B. M. Baughman, K. Bechtol, D. Bédérède, F. Bellardi, R. Bellazzini, B. Berenji, G. F. Bignami, D. Bisello, E. Bissaldi, R. D. Blandford, E. D. Bloom, J. R. Bogart, E. Bonamente, J. Bonnell, A. W. Borgland, A. Bouvier, J. Bregeon, A. Brez, M. Brigida, P. Bruel, T. H. Burnett, G. Busetto, G. A. Caliandro, R. A. Cameron, P. A. Caraveo, S. Carius, P. Carlson, J. M. Casandjian, E. Cavazzuti, M. Ceccanti, C. Cecchi, E. Charles, A. Chekhtman, C. C. Cheung, J. Chiang, R. Chipaux, A. N. Cillis, S. Ciprini, R. Claus, J. Cohen-Tanugi, S. Condamoor, J. Conrad, R. Corbet, L. Corucci, L. Costamante, S. Cutini, D. S. Davis, D. Decotigny, M. DeKlotz, C. D. Dermer, A. de Angelis, S. W. Digel, E. do Couto e Silva, P. S. Drell, R. Dubois, D. Dumora, Y. Edmonds, D. Fabiani, C. Farnier, C. Favuzzi, D. L. Flath, P. Fleury, W. B. Focke, S. Funk, P. Fusco, F. Gargano, D. Gasparrini, N. Gehrels, F. X. Gentit, S. Germani, B. Giebels, N. Giglietto, P. Giommi, F. Giordano, T. Glanzman, G. Godfrey, I. A. Grenier, M. H. Grondin, J. E. Grove, L. Guillemot, S. Guiriec, G. Haller, A. K. Harding, P. A. Hart, E. Hays, S. E. Healey, M. Hirayama, L. Hjalmarsdotter, R. Horn, R. E. Hughes, G. Jóhannesson, G. Johansson, A. S. Johnson, R. P. Johnson, T. J. Johnson, W. N. Johnson, T. Kamae, H. Katagiri, J. Kataoka, A. Kavelaars, N. Kawai, H. Kelly, M. Kerr, W. Klamra, J. Knödlseder, M. L. Kocian, N. Komin, F. Kuehn, M. Kuss, D. Landriu, L. Latronico, B. Lee, S. H. Lee, M. Lemoine-Goumard, A. M. Lionetto, F. Longo, F. Loparco, B. Lott, M. N. Lovellette, P. Lubrano, G. M. Madejski, A. Makeev, B. Marangelli, M. M. Massai, M. N. Mazziotta, J. E. McEnery, N. Menon, C. Meurer, P. F. Michelson, M. Minuti, N. Mirizzi, W. Mitthumsiri, T. Mizuno, A. A. Moiseev, C. Monte, M. E. Monzani, E. Moretti, A. Morselli, I. V. Moskalenko, S. Murgia, T. Nakamori, S. Nishino, P. L. Nolan, J. P. Norris, E. Nuss, M. Ohno, T. Ohsugi, N. Omodei, E. Orlando, J. F. Ormes, A. Paccagnella, D. Paneque, J. H. Panetta, D. Parent, M. Pearce, M. Pepe, A. Perazzo, M. Pesce-Rollins, P. Picozza, L. Pieri, M. Pinchera, F. Piron, T. A. Porter, L. Poupard, S. Rainò, R. Rando, E. Rapposelli, M. Razzano, A. Reimer, O. Reimer, T. Reposeur,

L. C. Reyes, S. Ritz, L. S. Rochester, A. Y. Rodriguez, R. W. Romani, M. Roth, J. J. Russell, F. Ryde, S. Sabatini, H. F. W. Sadrozinski, D. Sanchez, A. Sander, L. Sapozhnikov, P. M. Saz Parkinson, J. D. Scargle, T. L. Schalk, and G. Scolieri. The Large Area Telescope on the Fermi Gamma-Ray Space Telescope Mission. , 697(2):1071–1102, June 2009. doi: 10.1088/0004-637X/697/2/1071.

L. Bouchet, P. Mandrou, J. P. Roques, G. Vedrenne, B. Cordier, A. Goldwurm, F. Lebrun, J. Paul, R. Sunyaev, E. Churazov, M. Gilfanov, M. Pavlinsky, S. Grebenev, G. Babalyan, I. Dekhanov, and N. Khavenson. SIGMA Discovery of Variable E +- E - Annihilation Radiation from the Near Galactic Center Variable Compact Source 1E 1740.7-2942. , 383:L45, December 1991. doi: 10.1086/186237.

S. De Gaetano, L. Di Venere, F. Gargano, F. Loparco, L. Lorusso, M. N. Mazziotta, G. Panzarini, R. Pillera, and D. Serini. Constraints on the Gamma-Ray Emission from Small Solar System Bodies with the Fermi Large Area Telescope Data. , 951(1):13, July 2023. doi: 10.3847/1538-4357/acd5ce.

Roland Diehl, Thomas Siegert, Jochen Greiner, Martin Krause, Karsten Kretschmer, Michael Lang, Moritz Pleintinger, Andrew W. Strong, Christoph Weinberger, and Xiaoling Zhang. INTEGRAL/SPI γ-ray line spectroscopy. Response and background characteristics. , 611:A12, March 2018. doi: 10.1051/0004-6361/201731815.

J. S. Dohnanyi. Collisional Model of Asteroids and Their Debris. , 74:2531–2554, May 1969. doi: 10.1029/JB074i010p02531.

V. V. Emel'Yanenko, D. J. Asher, and M. E. Bailey. The fundamental role of the Oort cloud in determining the flux of comets through the planetary system. , 381(2):779–789, October 2007. doi: 10.1111/j.1365-2966.2007.12269.x.

M. Gilfanov, R. Syunyaev, E. Churazov, M. Pavlinskii, S. Grebenev, R. Kremnev, K. Sukhanov, N. Kuleshova, A. Goldwurm, J. Ballet, B. Cordier, J. Paul, M. Denis, L. Bouchet, D. Barret, and J. P. Roques. Observations of Nova MUSCAE with the Sigma Telescope on the GRANAT Observatory - Spectroscopic Properties in Hard X-Rays and Discovery of the Annihilation Line in the Spectrum. *Soviet Astronomy Letters*, 17:437, November 1991.

N. Guessoum, P. Jean, and W. Gillard. The lives and deaths of positrons in the interstellar medium. , 436(1):171–185, June 2005. doi: 10.1051/0004-6361:20042454.

H Halloin. |spimodfit| Explanatory Guide and Users Manual, version 2.9 edn., Max Planck Institut für extraterrestrische Physik. 2009.

R. C. Haymes, D. V. Ellis, G. J. Fishman, S. W. Glenn, and J. D. Kurfess. Observation of Hard Radiation from the Region of the Galactic Center. , 157:1455, September 1969. doi: 10.1086/150164.

P. Jean, J. Knödlseder, V. Lonjou, M. Allain, J. P. Roques, G. K. Skinner, B. J. Teegarden, G. Vedrenne, P. von Ballmoos, B. Cordier, P. Caraveo, R. Diehl, Ph. Durouchoux, P. Mandrou, J. Matteson, N. Gehrels, V. Schönfelder, A. W. Strong, P. Ubertini, G. Weidenspointner, and C. Winkler. Early SPI/INTEGRAL measurements of 511 keV line emission from the 4th quadrant of the Galaxy. , 407:L55–L58, August 2003. doi: 10.1051/0004-6361:20031056.

P. Jean, J. Knödlseder, W. Gillard, N. Guessoum, K. Ferrière, A. Marcowith, V. Lonjou, and J. P. Roques. Spectral analysis of the galactic e+e- annihilation emission. *Astronomy amp; Astrophysics*, 445(2):579–589, December 2005. ISSN 1432-0746. doi: 10.1051/0004-6361:20053765. URL `http://dx.doi.org/10.1051/0004-6361:20053765`.

G. V. Jung, D. J. Kurfess, W. N. Johnson, R. L. Kinzer, J. E. Grove, M. S. Strickman, W. R. Purcell, D. A. Grabelsky, and M. P. Ulmer. OSSE observations of 1E 1740.7-2942 in 1992 September. , 295:L23–L26, March 1995.

J. Knödlseder, P. Jean, V. Lonjou, G. Weidenspointner, N. Guessoum, W. Gillard, G. Skinner, P. von Ballmoos, G. Vedrenne, J. P. Roques, S. Schanne, B. Teegarden, V. Schönfelder, and C. Winkler. The all-sky distribution of 511 keV electron-positron annihilation emission. , 441(2):513–532, October 2005. doi: 10.1051/0004-6361:20042063.

H. A. Krimm, S. T. Holland, R. H. D. Corbet, A. B. Pearlman, P. Romano, J. A. Kennea, J. S. Bloom, S. D. Barthelmy, W. H. Baumgartner, J. R. Cummings, N. Gehrels, A. Y. Lien, C. B. Markwardt, D. M. Palmer, T. Sakamoto, M. Stamatikos, and T. N. Ukwatta. The Swift/BAT Hard X-Ray Transient Monitor. , 209(1):14, November 2013. doi: 10.1088/0067-0049/209/1/14.

Kenneth J. Mighell. Parameter Estimation in Astronomy with Poisson-distributed Data. I.The χ^2_γ Statistic. , 518(1):380–393, June 1999. doi: 10.1086/307253.

I. V. Moskalenko and T. A. Porter. The Gamma-Ray Albedo of the Moon. In *39th Annual Lunar and Planetary Science Conference*, Lunar and Planetary Science Conference, page 2300, March 2008.

Igor V. Moskalenko, Troy A. Porter, Seth W. Digel, Peter F. Michelson, and Jonathan F. Ormes. A Celestial Gamma-Ray Foreground Due to the Albedo of Small Solar System

Bodies and a Remote Probe of the Interstellar Cosmic-Ray Spectrum. , 681(2):1708–1716, July 2008. doi: 10.1086/588425.

Ramesh Narayan and Rajaram Nityananda. Maximum entropy image restoration in astronomy. , 24:127–170, January 1986. doi: 10.1146/annurev.aa.24.090186.001015.

N. Prantzos, C. Boehm, A. M. Bykov, R. Diehl, K. Ferrière, N. Guessoum, P. Jean, J. Knoedlseder, A. Marcowith, I. V. Moskalenko, A. Strong, and G. Weidenspointner. The 511 keV emission from positron annihilation in the Galaxy. *Reviews of Modern Physics*, 83(3):1001–1056, July 2011. doi: 10.1103/RevModPhys.83.1001.

W. R. Purcell, L. X. Cheng, D. D. Dixon, R. L. Kinzer, J. D. Kurfess, M. Leventhal, M. A. Saunders, J. G. Skibo, D. M. Smith, and J. Tueller. OSSE Mapping of Galactic 511 keV Positron Annihilation Line Emission. , 491(2):725–748, December 1997. doi: 10.1086/304994.

J. P. Roques, S. Schanne, A. von Kienlin, J. Knödlseder, R. Briet, L. Bouchet, Ph. Paul, S. Boggs, P. Caraveo, M. Cassé, B. Cordier, R. Diehl, P. Durouchoux, P. Jean, P. Leleux, G. Lichti, P. Mandrou, J. Matteson, F. Sanchez, V. Schönfelder, G. Skinner, A. Strong, B. Teegarden, G. Vedrenne, P. von Ballmoos, and C. Wunderer. SPI/INTEGRAL in-flight performance. , 411:L91–L100, November 2003. doi: 10.1051/0004-6361:20031501.

Thomas Siegert. The Positron Puzzle. , 368(4):27, April 2023. doi: 10.1007/s10509-023-04184-4.

Thomas Siegert. Time-variable diffuse γ-ray foreground. , 533(1):165–183, September 2024. doi: 10.1093/mnras/stae1742.

Thomas Siegert, Roland Diehl, Gerasim Khachatryan, Martin G. H. Krause, Fabrizia Guglielmetti, Jochen Greiner, Andrew W. Strong, and Xiaoling Zhang. Gamma-ray spectroscopy of positron annihilation in the Milky Way. , 586:A84, February 2016. doi: 10.1051/0004-6361/201527510.

Thomas Siegert, Roland M. Crocker, Roland Diehl, Martin G. H. Krause, Fiona H. Panther, Moritz M. M. Pleintinger, and Christoph Weinberger. Constraints on positron annihilation kinematics in the inner Galaxy. , 627:A126, July 2019a. doi: 10.1051/0004-6361/201833856.

Thomas Siegert, Roland Diehl, Christoph Weinberger, Moritz M. M. Pleintinger, Jochen Greiner, and Xiaoling Zhang. Background modelling for γ-ray spectroscopy with INTEGRAL/SPI. , 626:A73, June 2019b. doi: 10.1051/0004-6361/201834920.

Thomas Siegert, Joanna Berteaud, Francesca Calore, Pasquale D. Serpico, and Christoph Weinberger. Diffuse Galactic emission spectrum between 0.5 and 8.0 MeV. , 660:A130, April 2022. doi: 10.1051/0004-6361/202142639.

Gerry Skinner, Roland Diehl, Xiao-Ling Zhang, Latifa Bouchet, and Pierre Jean. The galactic distribution of the 511 kev e+/e- annihilation radiation. page 054, 03 2014. doi: 10.22323/1.228.0054.

D. M. Smith, M. Leventhal, R. Cavallo, N. Gehrels, J. Tueller, and G. Fishman. Limits on Reported Transient Emission Events near 0.5 MeV from the Crab and 1E 1740.7-2942. , 458:576, February 1996. doi: 10.1086/176840.

John Tomsick, Andreas Zoglauer, Clio Sleator, Hadar Lazar, Jacqueline Beechert, Steven Boggs, Jarred Roberts, Thomas Siegert, Alex Lowell, Eric Wulf, Eric Grove, Bernard Phlips, Terri Brandt, Alan Smale, Carolyn Kierans, Eric Burns, Dieter Hartmann, Mark Leising, Marco Ajello, Chris Fryer, Mark Amman, Hsiang-Kuang Chang, Pierre Jean, and Peter von Ballmoos. The Compton Spectrometer and Imager. In *Bulletin of the American Astronomical Society*, volume 51, page 98, September 2019. doi: 10.48550/arXiv.1908.04334.

G. Vedrenne, J. P. Roques, V. Schönfelder, P. Mandrou, G. G. Lichti, A. von Kienlin, B. Cordier, S. Schanne, J. Knödlseder, G. Skinner, P. Jean, F. Sanchez, P. Caraveo, B. Teegarden, P. von Ballmoos, L. Bouchet, P. Paul, J. Matteson, S. Boggs, C. Wunderer, P. Leleux, G. Weidenspointner, Ph. Durouchoux, R. Diehl, A. Strong, M. Cassé, M. A. Clair, and Y. André. SPI: The spectrometer aboard INTEGRAL. , 411:L63–L70, November 2003. doi: 10.1051/0004-6361:20031482.

Pauli Väisänen, Ilya Usoskin, Riikka Kähkönen, Sergey Koldobskiy, and Kalevi Mursula. Revised reconstruction of the heliospheric modulation potential for 1964–2022. *Journal of Geophysical Research: Space Physics*, 128(4):e2023JA031352, 2023. doi: https://doi.org/10.1029/2023JA031352. URL `https://agupubs.onlinelibrary.wiley.com/doi/abs/10.1029/2023JA031352`. e2023JA031352 2023JA031352.

S. S. Wilks. The Large-Sample Distribution of the Likelihood Ratio for Testing Composite Hypotheses. *The Annals of Mathematical Statistics*, 9(1):60 – 62, 1938. doi: 10.1214/aoms/1177732360. URL `https://doi.org/10.1214/aoms/1177732360`.

C. Winkler, T. J. L. Courvoisier, G. Di Cocco, N. Gehrels, A. Giménez, S. Grebenev, W. Hermsen, J. M. Mas-Hesse, F. Lebrun, N. Lund, G. G. C. Palumbo, J. Paul, J. P. Roques, H. Schnopper, V. Schönfelder, R. Sunyaev, B. Teegarden, P. Ubertini, G. Vedrenne, and A. J. Dean. The INTEGRAL mission. , 411:L1–L6, November 2003. doi: 10.1051/0004-6361:20031288.

Hiroki Yoneda, Thomas Siegert, and Saurabh Mittal. Imaging the positron annihilation line with 20-year INTEGRAL/SPI observations. *arXiv e-prints*, art. arXiv:2509.01066, September 2025. doi: 10.48550/arXiv.2509.01066.

Eidesstattliche Erklärung

Hiermit erkläre ich, dass ich die vorliegende Arbeit eigenständig und ohne fremde Hilfe angefertigt habe. Textpassagen, die wörtlich oder dem Sinn nach auf Publikationen oder Vorträgen anderer Autoren beruhen, sind als solche kenntlich gemacht. Die Arbeit wurde bisher keiner anderen Prüfungsbehörde vorgelegt und auch noch nicht veröffentlicht.

Würzburg, 02.10.2025

Rudi Reinhardt